Carl von Ossietzky
Universität Oldenburg

Studiengang Engineering Physics
Institut für Physik

MASTERARBEIT Titel

Efficiency Analysis of an
Air–Sand Heat Exchanger
for selected operating conditions
based on CFD–DEM Simulation

vorgelegt von Jacqueline McLeod (2198207)

Betreuer (SIJ): Dipl.–Ing. Cristiano Teixeira Boura
Erstgutachter: Prof. Dr. Jürgen Parisi
Zweitgutachter: Hans–Gerhard Holtorf
Oldenburg

Abstract

Air–Sand Heat Exchanger enable direct contact heat transfer between a fluid and a bulk solids. In simplified numerical simulations the interaction is described solely with Computational Fluid Dynamics as flow through a porous media. This approach neglects the impact of the fluid flow on the particle arrangement and resulting effects on the particle flow, which are important factors for the heat transfer. To overcome this inaccuracy a numerical simulation with Computational Fluid Dynamics to describe the continuum body of the fluid, and with the Discrete Element Method to describe the single particle based bulk solids was set–up. With this coupled simulation the fluid–particle interaction could be described and it showed that it cannot be neglected when setting the operating conditions, as the fluid–particle interaction and the possibly resulting effects pinning, blistering, and blocking have a major impact on the heat transfer efficiency.

Zusammenfassung

Luft–Sand Wärmetauscher ermöglichen den direkten Wärmeübergang zwischen einem Fluid und einem Schüttgut. In vereinfachten Simulationen wird die Wechselbeziehung mit reiner Computational Fluid Dynamics als Strömung durch ein poröses Medium beschrieben. Diese Herangehensweise vernachlässigt jedoch die Auswirkungen des Fluidstroms auf den Teilchenstrom und den daraus resultierenden Effekten, welche wichtige Faktoren für den Wärmeübergang darstellen. Für eine genauere Darstellung des Problems wurde eine numerische Simulation mit Computational Fluid Dynamics zur Beschreibung des Kontinuumskörpers Fluid und die Diskrete Elemente Methode zur Beschreibung des Teilchen basierten Schüttgutes erstellt. Mit dieser gekoppelten Simulation konnten die Fluid–Teilchen Wechselwirkungen beschrieben werden. Zusätzlich wurde gezeigt, dass diese Wechselwirkungen bei der Einstellung der Betriebsbedingungen vernachlässigt werden dürfen, da sie zu den Effekten Pinning, Blistering und Blocking führen und damit den Wärmeübergang empfindlich stören können.

Contents

List of Figures

List of Tables

Notation

Abbreviations

2D	Two dimensional
3D	Three dimensional
CAD	Computer–aided design
CFD	Computational Fluid Dynamics
CFL	Courant–Friedrichs–Levy Condition
coeff.	Coefficient
CSP	Concentrating Solar Power
DEM	Discrete Element Method
HiTExStor	High Temperature Heat Exchange and Storage
hxz	Heat exchange zone
IEA	International Energy Agency
LAMMPS	Large–scale Atomic/Molecular Massively Parallel Simulator
LIGGGHTS	LAMMPS Improved for general granular and granular heat transfer simulations
NSE	Navier–Stokes Equations
OpenFOAM	Open Source Field Operation and Manipulation
p–p	Particle–particle
SIJ	Solar Institute Jülich
UNFCCC	United Nations Framework Convention on Climate Change
VA3	Versuchsanlage (test facility) 3
VA4	Versuchsanlage (test facility) 4
w–p	Wall–particle

Symbols

A	area	m^2
Bi	Biot number	$-$
$\dot{C}$	heat capacity rate	$\mathrm{W\,K^{-1}}$
c	CFL factor	$-$
c_p	isobaric specific heat capacity	$\mathrm{J\,kg^{-1}\,K}$

d_k	equivalent particle diameter	m
de	depth	m
E	stress–strain modulus	$\mathrm{N\,m^{-2}}$
e	specific internal energy	$\mathrm{J\,kg^{-1}}$
$\dot{E}$	exergy	W
$\vec{F}$	force	N
f_a	form factor for bulk solids	—
f_{red}	reduction factor	—
G	shear modulus	$\mathrm{N\,m^{-2}}$
$\vec{g}$	gravity vector	$\mathrm{m\,s^{-2}}$
h	height	m
h_p	overlap	m
k	stiffness	$\mathrm{N\,m^{-1}}$
L	characteristic length	m
$\dot{m}$	mass flow	$\mathrm{g\,s^{-1}}$
$\vec{n}$	normal vector	—
NTU	Number of Transfer Units	—
Nu	Nusselt number	—
P	temperature effectiveness	—
p	pressure	Pa
Pr	Prandtl number	—
$\dot{Q}$	heat flow	W
$\dot{q}_s$	specific heat flow	$\mathrm{W\,kg^{-1}}$
R	heat capacity rate ratio	—
r	radius	m
Re	Reynold number	—
$\dot{S}$	entropy	$\mathrm{W\,K^{-1}}$
T	temperature	K
t	time	s
U	thermal conductance	$\mathrm{W\,m^{-2}\,K^{-1}}$
u	velocity	$\mathrm{m\,s^{-1}}$
w	width	m
x	simulation mesh cell width	m
α	heat transfer coefficient	$\mathrm{W\,m^{-2}\,K^{-1}}$

δ_{el}	tangential elastic displacement	m
η	dynamic viscosity	$\mathrm{Pa\,s}$
η_{ex}	exergetic efficiency	—
ϑ'	inlet temperature	K
ϑ''	outlet temperature	K
κ	heat capacity ratio	—
λ	thermal conductivity	$\mathrm{W\,m^{-1}\,K^{-1}}$
μ	Poisson ratio	—
ν	kinematic viscosity	$\mathrm{m^2\,s^{-1}}$
ρ	density	$\mathrm{kg\,m^{-3}}$
Ψ	void fraction	—

Indices

α	particle α
β	particle β
Ψ	related to void fraction
1	point 1
12	from point 1 to point 2
2	point 2
amb	ambient (temperature)
bs	bulk solids
c	collision
CFL	Courant–Friedrichs–Levy
eff	effective
f	fluid
free	superficial (velocity)
hxz	heat exchange zone
in	inlet (temperature)
lam	laminar
n	normal
out	outlet (temperature)
p	particle
R	Rayleigh
S	surface

sp	single particle
t	tangential
tot	total
turb	turbulent

1 Introduction

The last decades saw a growing awareness for energy demand development, power generation and their impact on the environment. In 1992 this lead to a combined effort of 196 countries to control the effects, and the United Nations Framework Convention on Climate Change (UNFCCC) treaty was established, from which the Kyoto Protocol from 1997 arose [29]. The aim of the UNFCCC treaty is to globally reduce energy related greenhouse emissions. The International Energy Agency (IEA) publishes annually the *World Energy Outlook* that depicts the political, economic and environmental impact of current energy and environmental politics in a long term analysis. The *World Energy Outlook* of 2012 for the period 2012 to 2035 prognoses a global temperature increase of 2 °C from 2012 to 2035, due to an increase in energy demand and fossil fuels being the dominant sources with a share of 80 % [1]. To reduce these negative effects the IEA provides an analysis of possible measures for key executives, for example further development of the renewable energies' sector. A promising element of this sector is the solar thermal power generation with a focus on Concentrating Solar Power (CSP). As the name implies, the CSP technology concentrates the solar radiance at one point to heat up a heat carrier medium. Thus, high temperatures can be achieved which are then further used for steam generation and subsequently power generation.

In 2010 the International Energy Agency [13] stated, that CSP in regions with strong direct normal radiance has great potential to become an important provider of renewable energy [cf. 13, p. 5]. But due to its dependence on solar radiance this technology underlies fluctuations, day–time and seasonal, which, in regards to the energy politics rule of energy security, must be compensated. To achieve this an efficient storage system for high operating temperatures is needed.

1.1 Solar Institute Jülich

The Solar Institute Jülich (SIJ) is an affiliated scientific facility of the University of Applied Sciences Aachen. It was founded in 1992 and has set its main focus on solar technologies ranging from small–scale thermal energy applications for domestic use to large–scale solar power plants.

Within the High Temperature Heat Exchange and Storage Project (HiTExStor Project) a new heat exchanger concept for CSP applications was developed. The aim of this project was to design an efficient heat exchanging system based on non–liquid heat carrier and

storage media, as these are typically chemically and physically stable for high temperatures and more cost efficient. For these heat exchangers different types of solids have been analysed for their respective thermal properties and for applicable procedures of transportation.

The current stage of development is the Air–Sand Heat Exchanger, which will be introduced in the following section.

1.2 Design and Working Principles of the Air–Sand Heat Exchanger

The most recent design of the Air–Sand Heat Exchanger is a circular form. But due to its closed set–up experimental observations regarding granular flow effects could not be carried out for this model. Therefore, the following work on the fundamentals for the development of a simulation set–up for the Air–Sand Heat Exchanger is based on the preceding rectangular model *VA3*. This model is a single–pass cross flow exchanger with both flows mixed, a symmetric stream, and of a basic rectangular design. It uses air as the heat carrier and sand as the storage medium.
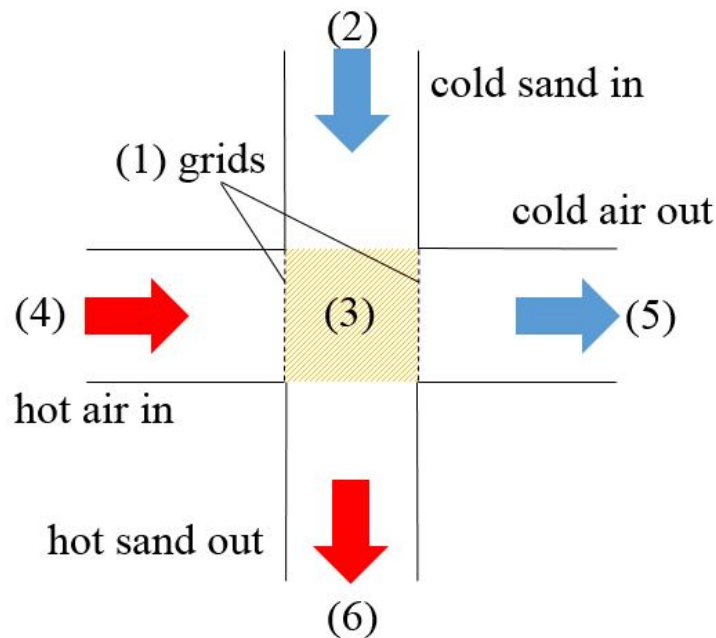

Fig. 1.1: Simplified set–up of a rectangular Air–Sand Heat Exchanger with cross flow. ① grids, ② sand inlet, ③ heat exchange zone, ④ air inlet, ⑤ air outlet and ⑥ sand outlet.

The simplified set–up of the experimental heat exchanger *VA3* is shown in Fig. 1.1. It consists of two ducts perpendicular to each other. The intersection of both ducts forms the heat exchange zone ③, in which the major portion of heat transfer occurs. The heat carrier flow (air) is forced horizontally through the sand in the heat exchange zone via a downstream suction pump. To prevent sand from entering the air duct (and consequentially the suction pump) fine separating grids ① are installed on the inlet (④) and outlet (⑤) sides of the heat exchange zone in air flow direction. The heat storage medium (sand) on the other hand flows vertically down the duct due to gravitational force. Nevertheless, the sand does not fall freely, its mass flow and therefore the velocity of the particles is dictated by the dimensions of the outlet hopper at the bottom of the sand duct. During the charging process the sand would be supplied by the cold storage tank. Following this procedure the sand is heated up while running through the heat exchange zone, and then passed on to the hot storage tank, as indicated in Fig. 1.1 (p. 2). The opposite arrangement of above stated configuration will therefore apply for the process of discharging the stored medium (heated sand)..

This cross flow design with both flows mixed makes it important to investigate the interaction between the air and the sand. First of all, the sand grains reduce the air flow cross section considerably, leading to a pressure difference, which has to be compensated. In addition to this, it has been observed during the experiments that high air mass flows had significant impacts on the sand mass flow behaviour.

To be able to analyse this behaviour of alternating air and sand mass flows without constant changes in experimental set–ups and equipment, a numerical simulation is to be derived. The simulation has to be able to describe the pressure difference caused by the sand column and the impact of different air mass flows on the sand mass flow. As the pressure difference caused by the separating grids is significantly smaller in comparison, the grids are to be neglected within the simulation. Secondary, the simulation is to be able to calculate the heat transfer process. As the Air–Sand Heat exchanger is a direct–contact heat exchanger, the main focus lies on convective heat transfer. Thermal conduction can be neglected, as no separating bodies, e.g. walls, have to be considered. Also thermal radiation can be neglected.

All experimental observations regarding the heat exchanger set–up *VA3* have been taken from the experimental work by Niederwestberg [21].

The outline of this Master thesis is to first summarise the aspects of the Air–Sand Heat Exchanger which are to be analysed and the chosen approach. Chapter 3 provides the theoretical background for a numerical and analytical assessment of fluid and particle flow behaviour and heat transfer, and introduces open source software applicable for the sought investigations. Chapter 4 illustrates the modelling of the simulation boxes and

the determination of boundary conditions for the CFD and the DEM simulation. It also provides all settings needed for the investigated operating conditions and indicates important differences. The results chapter focusses on the validation of the coupled CFD and DEM simulation and on identifying major impact factors on particle flow behaviour. In addition, it demonstrates the importance of the particle flow behaviour for the heat exchange process. To conclude this thesis, the most significant notes and major findings of this work are summarised in chapter "6 Conclusion".

2 Scope of Work

As concluded in the previous chapter, the main focus of this work lies on the development of a simulation concept for the Air–Sand Heat Exchanger. This concept is to include methods to describe fluid and granular flow behaviour and heat transfer. The objective is to be able to analyse the efficiency of the Air–Sand Heat Exchanger including pressure differences and their effects on the sand flow. The development process is divided into 5 steps:

- The first step includes the assessment of suitable programmes for fluid flow and inter–particle forces simulation.

- During the second step the programmes are to be applied, Computer–aided design (CAD) models of the heat exchanger created and the simulation box (including calculation grid) defined.

- The next step is to validate the prepared simulation based on the measurements obtained from the experimental heat exchanger *VA3*.

- Step four is the comparison of the simulation results with the observations made with the heat exchanger *VA3* regarding the granular flow effects pinning, blistering and blocking, and other particle flow behaviour, with the simulation output.

- The fifth step is to conduct a sensitivity analysis for certain material properties, as the correct properties for the materials used in the experiments are not known.

- The last step number six is the application of the simulation concept on a heat transfer case with selected pressure difference effects and to qualitatively compare the simulation results regarding the heat exchanger efficiency.

The findings of this work concerning granular flow effects and the influence of material properties are to be used for a circular heat exchanger design in remote future.

3 Theory

In order to conduct a simulation the theoretical background of the analysed problem must be established and adequate physical, mathematical or numerical models chosen to describe the problem in as much detail as needed and possible for an acceptable solution [cf. 31, p. 10]. The theoretical models that are used to describe the problem of the heat exchanger behaviour are introduced in the following sections. The first section will contain numerical models, which form the basis of the simulations. In contrast to this the second section provides analytical methods, which are used to describe effects when measured data is missing, or to compare simulation results with model expectations.

3.1 Definitions

Before the theoretical background for the numerical and analytical investigation of a Air–Sand Heat Exchanger is presented, there will first be a short introduction to granular flow effects that form the basis for this work. There are three effects that can be observed for specific operating conditions: pinning, blistering, and blocking, as depicted in Fig. 3.1.
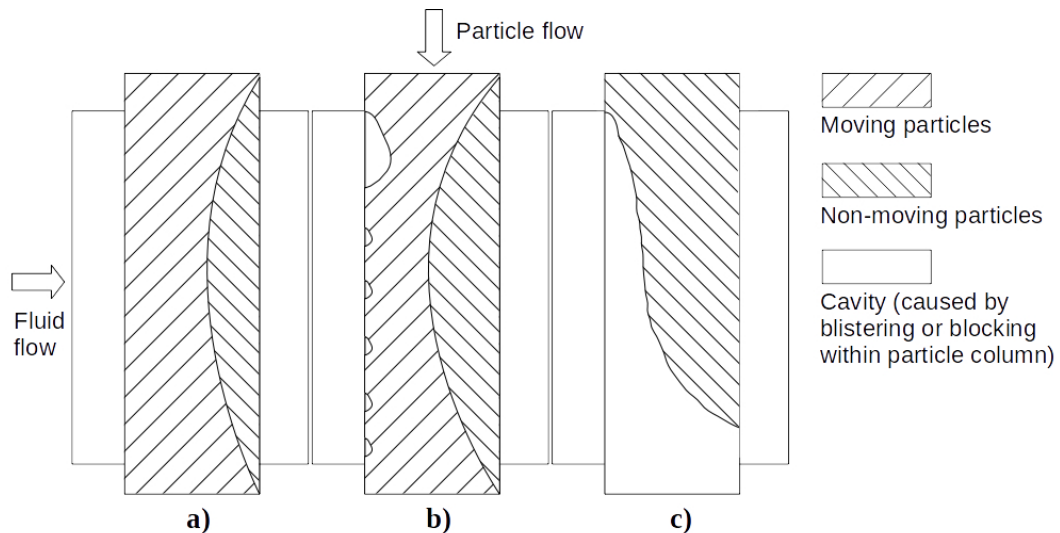
Fig. 3.1: Schematic of granular flow effects: **a)** Pinning, **b)** Blistering, **c)** Blocking. Fluid flows from left to right, particle flow from top to bottom. [cf. 22, p. 2538]

Pinning is the effect when particles on the fluid outlet side of the granular column cease to move. The particles form a *filter cake* on the separating mesh which grows in thickness with increasing fluid velocity.

Blistering occurs at higher velocities (and therefore higher pressure gradients) than pinning and is always accompanied by pinning. At the top of the fluid inlet area the granular flow breaks away from the separating grid and forms a small fluid bubble. With increasing fluid velocities the bubbles grow in size and numbers.

Blocking is the last stage of effected granular flow. In this stage the complete granular flow has come to a halt. The *filter cake* has reached its maximum extent and the remaining area was cleared by blistering effects. The *filter cake* blocks any further granular flow.

In the study of Pilcher and Bridgwater [22] it was found that these effects primarily depend on the granular material properties (size, friction coefficients, density, YOUNG'S MODULUS, . . .) and secondly on the velocities respectively the pressure gradient obtained [cf. 22, p. 2542].

The sizing of the flow ducts were found not to have any influence on the pressure gradients under which the effect's initial formation took place [cf. 22, p. 2540]. Only with the change of material properties would the pressure gradients for initialising effects alter.

3.2 Numerical Methods

As complex applications can seldom be solved analytically, numerical methods are applied. For example, the Air–Sand Heat Exchanger combines two different flow types with complex interactions that cannot be neglected. These circumstances lead to the requirement of a numerical analysis based on the respective physical properties and behaviour of the involved flows. In the case of the fluid mechanical problems the numerical solution is obtained through Computational Fluid Dynamics (CFD), whereas the granular behaviour is numerically described with the Discrete Element Method (DEM).

3.2.1 Computational Fluid Dynamics

3.2.1.1 Fundamentals – Navier–Stokes Equations

The CFD are based on the NAVIER–STOKES EQUATIONS (NSE), which are capable to describe the full range of time–dependent and time–independent flow behaviour, including small–scale eddies, turbulence and temperature changes. [cf. 18, p. 42] They consist of the

- *continuity equation*:

$$\frac{\partial}{\partial t}\left(\rho\right) + \nabla\left(\rho\vec{u}\right) = 0, \tag{3.1}$$

- the *momentum equation*

$$\frac{\partial}{\partial t}\left(\rho\vec{u}\right) + \left(\vec{u}\nabla\right)\vec{u} = \rho\vec{g} - \nabla p + \nu\rho\nabla^2\vec{u}, \tag{3.2}$$

- and the *conservation of energy*

$$\frac{\partial}{\partial t}\left[\rho\left(e + \frac{1}{2}\vec{u}^2\right)\right] + \nabla\left[\rho\vec{u}\left(h + \frac{1}{2}\vec{u}^2\right) - \left(\nu\rho\nabla^2\vec{u}\right)\vec{u} - \lambda\nabla T\right] = \rho\vec{g}\vec{u} + \rho\dot{q}_S \tag{3.3}$$

where p is the pressure, $\vec{g}$ the gravity vector, e the specific internal energy, h the height, $\dot{q}_S$ the thermal radiation, λ the thermal conduction, ν the kinetic viscosity and ρ the density. [cf. 18, p. 22 and p. 15]

Considering the "Scope of Work" and "Design and Working Principles of the Air–Sand Heat Exchanger" it is possible to undertake the first simplifications of the NSE. During the experimental work it was observed that compared with the temperature gradient the pressure change through the heat exchanger is negligible. This leads to the assumption that, at a constant temperature, the density changes under pressure are insignificant and incompressibility may be applied to the fluid air. Further, it simplifies the *continuity equation* to

$$\nabla\vec{u} = 0. \tag{3.4}$$

Nevertheless, the dependence of the density ρ on the temperature still must be considered. With Eq. (3.4) this reduces the *momentum equation* to

$$\rho\left(\frac{\partial}{\partial t}\vec{u} + \left(\vec{u}\nabla\right)\vec{u}\right) = \rho\vec{g} - \nabla p + \nu\rho\Delta\vec{u}. \tag{3.5}$$

For CFD the simplified equations are descretised into finite difference equations, according to the properties of the solution wanted [18, cf. chapter 3]. These are then solved for the nodes of the specified computing mesh.

3.2.1.2 Thermal Heat Transfer

The modified NAVIAR–STOKES EQUATIONS describe the actual flow behaviour, including energy distribution and general temperature changes. In order to simulate heat exchange though the existing model has to be extended to incorporate a heat transfer mode. As

previously stated the heat transfer process of interest is the convective heat transfer, which is described by NEWTON'S APPROACH [cf. 23, p. 31]:

$$\dot{Q} = \alpha A \left(T_S - T_\infty \right) \tag{3.6}$$

with T_S being the surface temperature of the solid, T_∞ the fluid temperature, and α the heat transfer coefficient.

The heat transfer coefficient is not a material property and the determination process due to the variety of its dependences complicated. Therefore, the heat coefficient is derived over the dimensionless NUSSELT NUMBER Nu (Eq. (3.7)), [cf. 23, p. 219–221]

$$Nu \equiv \frac{\alpha L}{\lambda} \tag{3.7}$$

with L the characteristic length the fluid flows past the NUSSELT NUMBER can be described as the correlation of the REYNOLD Re and PRANDTL NUMBER Pr [cf. 23, p. 220]

$$Nu = Nu \left(Re, Pr \right). \tag{3.8}$$

As the heat transfer between a fluid and a bulk solids is being investigated, the respective equations for the REYNOLD and PRANDTL NUMBER as well as the NUSSELT NUMBER itself have to be adjusted to accommodate the bulk solids void fraction Ψ. This leads to the modified equations of

$$Re_\Psi = \frac{u_{free} L}{\nu_f \, \Psi} \tag{3.9}$$

and

$$Pr = \frac{\eta_f c_{pf}}{\lambda_f} \tag{3.10}$$

with the superficial velocity u_{free} and the fluid dynamic viscosity η_f.

The NUSSELT NUMBER has to be attuned from the simple NUSSELT NUMBER for a single body (Eq. (3.7)) to a bulk solids'. The following Equations (3.11) to (3.13) describe the adaptation procedure as proposed by the model by GNIELINKSI. [cf. 30, p. 839]

$$Nu = f_a Nu_{sp} \tag{3.11}$$

Nu_{sp} (NUSSELT NUMBER for single particle) is defined as

$$Nu_{sp} = 2 + \sqrt{Nu_{lam}^2 + Nu_{turb}^2} \tag{3.12}$$

with

$$Nu_{lam} = 0.664\sqrt{Re_{\Psi}}\sqrt[3]{Pr} \quad \text{(a)} \qquad Nu_{turb} = \frac{0.037 Re_{\Psi}^{0.8} Pr}{1 + 2.443 Re_{\Psi}^{-0.1}\left(Pr^{\frac{2}{3}} - 1\right)}. \quad \text{(b)} \qquad (3.13)$$

f_a is the form factor to apply according to the particle type. For bulk solids with uniform spheres it is defined as

$$f_a = 1 + 1.5\left(1 - \Psi\right) \tag{3.14}$$

and the void fraction is described as

$$\Psi = \frac{\rho_{tot} - \rho_{bs}}{\rho_{tot}} \tag{3.15}$$

with the overall density ρ_{tot} and the bulk solids' density ρ_{bs} [cf. 11, p. 126].

3.2.1.3 Time Step – Courant–Friedrichs–Levy Condition

To run a stable transient simulation based on the discretised forms of the NSE, the computing mesh must fulfil the Courant–Friedrichs–Levy (CFL) condition. This condition states the number of cells a fluid particle with the velocity u passes during a set time step Δt_{CFL} and the set distance between the mesh's nodes Δx. For an explicit solver the simulation is only stable and able to converge when

$$c = \frac{u \Delta t_{CFL}}{\Delta x} \leq c_{max}, \tag{3.16}$$

with $c_{max} = 1$. For implicit solvers the CFL condition may increase up to $c_{max} = 10.000$. [cf. 18, p. 59]

The CFL condition is met by varying the time step Δt_{CFL}. In addition, the distance Δx may be varied, depending on the analysed problem and the resulting computing time.

3.2.2 Discrete Element Method

3.2.2.1 Fundamentals – Discrete Element Method

When analysing granular flow with a solid concentration above $50\,\%$ per volume ,it must be taken into account that the "forces are largely generated by inter particle contacts" [4, p. 209]. To incorporate the particle contact effects into the granular flow behaviour and to be able to describe bulk solids as collection of individual bodies the Discrete

ELEMENT METHOD is used. <u>Figure 3.2</u> shows the basic approach of DEM to describe the collision of two spheres and the resulting contact forces $\vec{F_c}$.
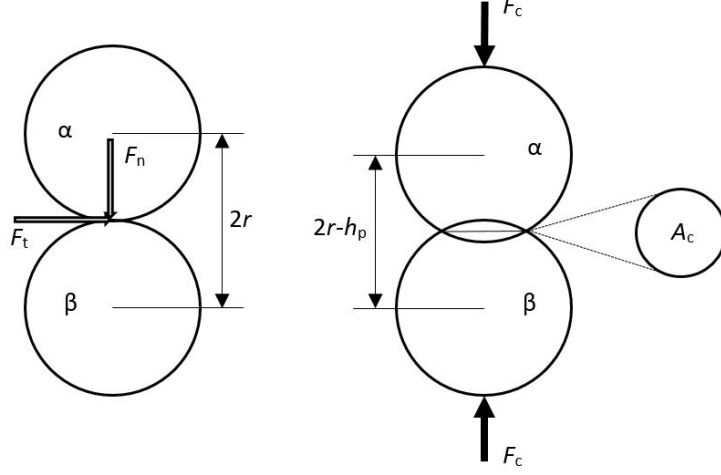
Fig. 3.2: Schematic of the collision of two spheres: Left before collision, right after collision. With contact force F_c and resulting overlap (deformation) h_p and contact area A_c [cf. 4, p. 209]

Generally, there are two approaches to formulate the outcome of the particle collision: HOOKE model for linear elasticity and HERTZ model for non–linear elasticity. Due to the fact that the collision area A_c and the caused strain change simultaneously during the deformation, a "non–linearity of the contact response" [4, p. 209] can be assumed. Therefore, only the HERTZ model is explained in the following.

The model contact forces $\vec{F_c}$ between particles α and β are made up of normal and tangential forces, $\vec{F_n}$ respectively $\vec{F_t}$, as shown in Eq. (3.17) [cf. 33, p. 268]:

$$\vec{F}_{c,\alpha\beta} = \vec{F}_{n,\alpha\beta} + \vec{F}_{t,\alpha\beta} \tag{3.17}$$

According to the HERTZ model the normal elastic contact can be described as

$$\vec{F}_{n,\alpha\beta} = \vec{n} \int_0^{h_p} k_n\left(h_p\right) dh_p = \vec{n}\frac{4}{3}E^{eff}\sqrt{r^{eff}}h_p^{(3/4)} \tag{3.18}$$

with the normal vector $\vec{n}$ and the normal interaction stiffness k_n

$$k_n\left(h_p\right) = 2E^{eff}\sqrt{r^{eff}}\sqrt{h_p} \tag{3.19}$$

in which r^{eff} is the effective radius (see Eq. (3.20)) of the contacting particles and h_p the overlap of both particles [cf. 33, p. 268].

$$r^{eff} = \frac{r_\alpha r_\beta}{r_\alpha + r_\beta} \tag{3.20}$$

Similar to the effective radius r^{eff} the effective stress–strain (YOUNG'S) modulus E^{eff} for the HERTZ model is determined as

$$E^{\mathit{eff}} = \frac{E_\alpha E_\beta}{E_\alpha \left(1 - \mu_\beta^2\right) + E_\beta \left(1 - \mu_\alpha^2\right)} \tag{3.21}$$

with the POISSON RATIO μ and the particle and wall indicators α and β [cf. 33, p. 268].

Describing the tangential force $\vec{F}_t$ is more complicated as it depends on the movement between two particles in respect to each other. Globally this dependence follows the MOHR–COULOMB behaviour and can be expressed as a contact with stick when $\vec{F}_{t,st} < \mu_f \vec{F}_n$. The tangential stick force is stated as the product of the negative tangential stiffness k_t and the tangential elastic displacement $\vec{\delta}_{el}$ (Eq. (3.22)) [cf. 33, p. 269].

$$\vec{F}_{t,st} = -k_t\left(t\right)\vec{\delta}_{el}\left(t\right) \tag{3.22}$$

The tangential stiffness itself is defined as

$$k_t\left(t\right) = 8G^{\mathit{eff}}\sqrt{r^{\mathit{eff}}}\sqrt{h_p\left(t\right)}. \tag{3.23}$$

with the equivalent shear modulus of both particles' materials G^{eff} (Eq. (3.24)) [cf. 33, p. 269].

$$G^{\mathit{eff}} = \frac{2}{3}\frac{G_\alpha G_\beta}{G\alpha\left(2 - \mu_\beta\right) + G_\beta\left(2 - \mu_\alpha\right)} \tag{3.24}$$

Together with the relation between the stress–strain modulus E, the shear modulus G and the POISSON ratio μ,

$$G = \frac{E}{2\left(1 + \mu\right)} \tag{3.25}$$

the Equations (3.18) to (3.24) form the basis for DEM analysis of dense flow of granular materials.

3.2.2.2 Time Step – Rayleigh Time

According to Sykut et al. [28] TIMOSHENKO & GOODIER found in 1970 that disturbances which occur due to particles in motion in a granular system "propagate in a form of Rayleigh waves along surface of solid" [28, p. 170]. The derived RAYLEIGH TIME is the time said surface wave takes to spread through the solid particle [cf. 27, p. 5]. The RAYLEIGH TIME Δt_R is expressed as

$$\Delta t_R = \frac{\pi r \sqrt{\frac{\rho_p}{G}}}{\left(0.1631\mu + 0.8766\right)}, \tag{3.26}$$

with the particle density ρ_p. The time step for DEM simulations depends on the Rayleigh Time. The standard values for DEM simulation time steps are in the range of $0.1\Delta t_R$ to $0.3\Delta t_R$ [cf. 27, p. 5].

3.3 Analytical Methods

The analytical methods provide tools to estimate the outcome of set operating conditions without the need of expensive experimental set–ups or complex simulations. In the following the analytical methods for determining pressure losses across particle beds, the heat transfer parameters of a known heat exchanger design, and the efficiency of a heat exchanger.

3.3.1 Ergun Equation

The analytical method to investigate the pressure drop along a non–moving packed bed of particles is the Ergun Equation. Its origin lies in Darcy's Law and the later works of Carman & Kozeny. In contrast to Darcy's Law it considers the turbulent components of pressure loss due to particles as well as laminar components. [cf. 24, p. 153–155]

$$\frac{(-\Delta p)}{w} = 150 \underbrace{\frac{\nu_f \rho_f u_{free}}{d_k^2} \frac{(1-\Psi)^2}{\Psi^3}}_{\substack{laminar \\ component}} + 1.75 \underbrace{\frac{\rho_f u_{free}^2}{d_k} \frac{(1-\Psi)}{\Psi^3}}_{\substack{turbulent \\ component}} \tag{3.27}$$

with the equivalent particle diameter d_k.

The component with the greater impact on the pressure gradient can be estimated by determining the Reynolds number Re (see Eq. (3.9)). For $Re_\Psi < 10$ fully laminar conditions exist and the *laminar component* dictates the pressure loss behaviour. As for $Re_\Psi > 2000$ fully turbulent flow exists and the *turbulent component* predicts the trend of the pressure loss. [cf. 24, p. 155]

3.3.2 Exergetic Efficiency of Heat Exchanger

The efficiency states the usefulness of a system, the simplest definition being the ratio of received energy to invested energy. But in the case of thermal energy further differentiation must be made. According to Hilfiker et al. [12] there are three different categories of energy quality (see Tab. 3.1, p. 14), depending on the energy's ability to be converted to

work. Table 3.1 shows clearly that thermal energy above ambient temperature consists of *exergy* and *anergy*. The *exergy* can be fully converted to work, whereas *anergy* cannot. In addition, the *exergy* part of the thermal energy increases with rising temperature. Therefore, to correctly define the efficiency of a heat exchanging system the exergy component of the thermal energy must be analysed. [cf. 12, p. 79]

Tab. 3.1: Categorisation of energy into form and quality classes [cf. 12, p. 77]

Category	**I**	**II**	**III**
Convertibility to work	total	partial	none
Form of energy	mechanical, electrical, chemical	thermal	thermal at T_{amb}
Quality of energy	exergy	exergy & anergy	anergy

The relation between thermal energy and *exergy* is depicted in Fig. 3.3. The heat flow $\dot{Q}$ on both sides of the wall is approximately identical, whereas the exergy $\dot{E}_Q$ is not. As the heat transfer is an irreversible process it leads to exergy losses $\dot{E}_L$, therefore decreases the exergy and increases the anergy of the thermal energy.
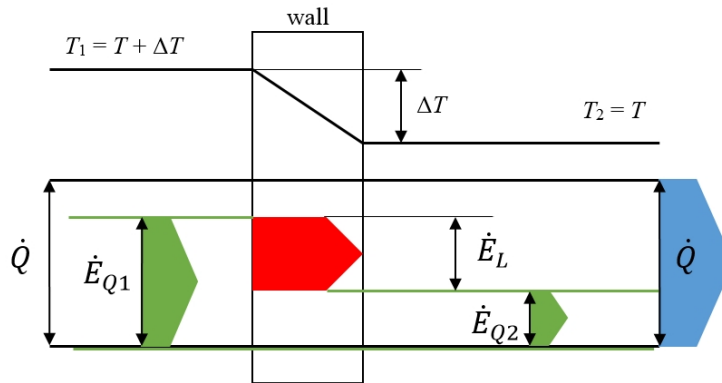
Fig. 3.3: Flow diagram of energy $\dot{Q}$ and exergy $\dot{E}_Q$ development for heat transfer through a wall. The exergy losses $\dot{E}_L$ are caused by irreversible heat transfer. [cf. 12, p. 80]

For a heat exchanger the *thermal exergy loss* as well as the *mechanical exergy loss* due to pressure gradients have to be considered. The *thermal exergy loss* must be analysed for all flows involved in the heat transfer (in this case air and sand). The thermal exergy loss is described as the difference of the exergy released (entropy reduction on hot side T_h) and the exergy gained (entropy rise on cold side T_c) between two points 1 and 2 in reference to a set temperature [cf. 5, p. 400]. The exergy of a heat transfer rate can therefore be described as

$$\dot{E}_{Q12} = \dot{Q}_{12} - T_{amb}\left(\dot{S}_2 - \dot{S}_1\right) \tag{3.28}$$

with the reference temperature T_{amb} and the entropy difference

$$\left(\dot{S}_2 - \dot{S}_1\right)_{thermal} = \dot{m}c_p \ln\left(\frac{T_2}{T_1}\right) \tag{3.29}$$

for isobar conditions [cf. 17, p. 116]. The heat transfer rate $\dot{Q}_{12}$ is described as

$$\dot{Q}_{12} = \dot{m}c_p\left(T_2 - T_1\right) \tag{3.30}$$

with $\dot{m}$ as the mass flow and c_p the heat capacity.

For the forced (pumped) flow the *mechanical exergy loss*, e.g. pressure losses, must be additionally analysed under isothermal conditions [cf. 17, p. 116]. This leads to the mechanical entropy difference for the forced flow:

$$\left(\dot{S}_2 - \dot{S}_1\right)_{mech} = -\dot{m}c_p \frac{\kappa - 1}{\kappa} \ln\left(\frac{p_2}{p_1}\right) \tag{3.31}$$

with the isotropic exponent κ. The mechanical entropy difference must be added to Eq. (3.29) when analysing the forced flow.

The exergetic efficiency η_{ex} is defined as the ratio of received exergy $\dot{E}_{out}$ and invested exergy $\dot{E}_{in}$ [cf. 5, p. 160]

$$\eta_{ex} = \frac{\dot{E}_{out}}{\dot{E}_{in}}. \tag{3.32}$$

Keeping in mind that the exergy gained by the storage medium (cold side) is crucial for further processes, it is defined as $\dot{E}_{out}$ and the exergy released by the heat carrier (hot side) as the invested exergy $\dot{E}_{in}$. These considerations assume charging and must therefore be adjusted when the exergetic efficiency of the discharge process is analysed, noting that the mechanical loss is always connected to the forced flow.

Altogether the exergetic efficiency analysis allows for a better assessment of the usefulness of a heat exchanging system for high operating temperatures and with the use of granular materials as storage medium. It accounts for the energy quality as well as for pressure effects caused by the granular material.

3.3.3 P–NTU Method

To be able to investigate the exergetic efficiency of a heat exchanger, the in- and outlet temperatures and the pressure gradient must be known (cf. 3.3.2). The analytical determination of the pressure gradient is shown in "3.3.1 Ergun Equation". For a known heat exchanger design the missing outlet temperatures are calculated based on dimensionless

numbers with the P–NTU Method. The P–NTU Method relates the temperature effectiveness P to the number of transfer units NTU [cf. 20, chap. 7]. In the following the P–NTU Method is introduced for a single–pass cross flow exchanger with both fluids mixed and a symmetric stream, as this case applies to the investigated heat exchanger set–up. For other set–ups refer to chapter 3 of Shah and Sekulić [26].

The relation between P and NTU is described as

$$\frac{1}{P_j} = \frac{1}{1 - exp\left(-NTU_j\right)} + \frac{R_j}{1 - exp\left(-R_j NTU_j\right)} - \frac{1}{NTU_j}, j = h, c.$$ (3.33)

The NTU is the ratio of the thermal conductance kA to the heat capacity rate C:

$$NTU_j = \frac{UA}{\dot{C}_j}$$ (3.34)

with the heat capacity rate as the product of the mass flow $\dot{m}$ and the heat capacity c_p:

$$\dot{C}_j = \dot{m}_j \bar{c}_{pj}.$$ (3.35)

The heat capacity rate ratio R is described as

$$R_h = \frac{\dot{C}_h}{\dot{C}_c} = \frac{1}{R_h}, 0 \leq R_h \leq \infty.$$ (3.36)

Inserting Equations (3.34) to (3.36) into Eq. (3.33) the temperature effectiveness is obtained, which leads with the known inlet temperatures ϑ_1' and ϑ_2'

$$P_h = \frac{\vartheta_h' - \vartheta_h''}{\vartheta_h' - \vartheta_c'} \quad \text{(a)} \qquad\qquad P_c = \frac{\vartheta_c'' - \vartheta_c'}{\vartheta_h' - \vartheta_c'} \quad \text{(b)}$$ (3.37)

to the outlet temperatures ϑ_1'' and ϑ_2'' of both flows. [cf. 20, chap. 7.1]

3.4 Simulation Software

The simulations are carried out with the software packages CFDEMcoupling (vers. 2.7.1), OpenFOAM (vers. 2.3.0) and LIGGGHTS (vers. 3.0.6) on a Linux operating system. A short overview of the working mechanisms is given in the following sections.

ParaView is used for post–processing, but not further mentioned, as no specific settings are necessary.

3.4.1 CFDEMcoupling

The software used for the simulation of the Air–Sand Heat Exchanger is the open source software CFDEMcoupling. CFDEMcoupling is distributed and continuously further developed by CFDEM®Project and was first released in 2010. It provides a framework for CFD–DEM coupled simulations based on the LIGGGHTS DEM code and the CFD package OpenFOAM [7]. This framework expands the OpenFOAM CFD solvers to "include a coupling to the DEM code LIGGGHTS" [7].

The CFDEMcoupling modifies the simplified NAVIER-STOKES EQUATIONS (see Eq. (3.4) and (3.5), p. 8) to accommodate the particle phase within the fluid phase. This is done by inserting the void fraction Ψ of the particle bed, and the momentum exchange $\vec{R}_{sl}$ between fluid and particle phase [cf. 9, p. 5]:

$$\frac{\partial \Psi}{\partial t} + \nabla \left(\Psi \vec{u} \right) = 0 \tag{3.38}$$

$$\frac{\partial \left(\Psi \vec{u}_f \right)}{\partial t} + \nabla \left(\Psi \vec{u}_f \vec{u}_f \right) = -\Psi \nabla \frac{p}{\rho_f} - \vec{R}_{sl} + \vec{g} + \nu \Delta \vec{u} \tag{3.39}$$

The momentum exchange is calculated for each cell. For $\Psi \leq 0.8$ it is derived from the Ergun Equation as follows [cf. 9, p. 5–6]:

$$\vec{R}_{sl} = \vec{K}_{sl} \left(\vec{u}_f - \vec{u}_p \right) \tag{3.40}$$

and

$$\vec{K}_{sl} = 150 \frac{\left(1 - \Psi \right)^2 \nu_f}{\Psi d_k^2} + 1.75 \frac{\left(1 - \Psi \right) \left| \vec{u}_f - \vec{u}_p \right|}{d_k}. \tag{3.41}$$

To solve the aforementioned equations (Eq. (3.38) to (3.41)) the CFDEMcoupling toolbox calls the respective solvers of the CFD and DEM software. In the first step the DEM code determines particle properties (position and velocity), in the next this data is transferred to the CFD code which then calculates the fluid properties and impacts (momentum exchange) on the particles. The output of these calculations are then returned to the DEM code to restart the solving process [cf. 9, p. 5]. The parameters that affect the data exchange are stated in "4.4 CFDEMcoupling – Merging the Models".

As the Air–Sand Heat Exchanger is to be analysed as having an incompressible transient flow with heat transfer the CFDEMcoupling model *cfdemSolverPisoScalar* is used. It calls the OpenFOAM *PISO* solver (see 3.4.2) and the DEM LIGGGHTS code (see 3.4.3).

In addition to modifying the NSE and calling the relevant CFD and DEM solver, the CFDEMcoupling determines further models which are to be applied to the investigated problem.

For the Air–Sand Heat Exchanger simulations these models are:

KochHillDrag is a force model to calculate the forces which act on each DEM particle
(e.g. particle–fluid interaction). Focus lies on the drag forces. [cf. 7, p. 23]

gradForce is a force model similar to KochHillDrag. Its focus lies on "the particle based
pressure gradient force" [7, p. 21]

viscForce is a force model which "calculates the particle based viscous force" [7, p. 34]

LaEuScalarTemp is a force model which does not affect the fluid–particle interaction.
It is used to calculate the heat flux between the fluid and particles [cf. 7, p. 24],
according to the convective heat transfer method described in "3.2.1.2 Thermal Heat
Transfer".

The CFDEMcouling consists of many more models, but these four models describe the
major influences on the investigated fluid and particle flows. Also, the CFDEMcoupling
software comes with four standard solvers, but additional solvers to for example incorpo-
rate porous sections can be implemented by the user.

3.4.2 CFD – OpenFOAM

Open Source Field Operation and Manipulation (OpenFOAM) is a C++ based CFD
simulation software. It is distributed by the OpenFOAM Foundation and was first released
in 2004. It contains all means for pre–processing (mesh generation), solving, and to output
data for post–processing. [8]

The OpenFOAM solvers include solvers for compressible, incompressible, stationary, tran-
sient and other flows. The CFDEMcoupling model calls the PISO solver. This pressure–
implicit split–operator (PISO) algorithm is used for transient problems "for solving equa-
tions for velocity and pressure" [8, U-124]. It solves the simplified NSE, the procedure for
this is initialised with pre–set values which are continuously corrected over several time
steps until the residuals meet the set convergence criteria.

Any thermal simulations are initialised by the CFDEMcoupling method, therefore no
additional settings of OpenFOAM are required.

A great advantage of the OpenFOAM software is the open source coding. The solvers'
coding is easily accessible and can be extended with user defined functions when needed.

3.4.3 DEM – LIGGGHTS

LIGGGHTS, LAMMPS[1] Improved for general granular and granular heat transfer simulations, is an open source software for DEM particle simulations [15]. It is distributed and continuously further developed by CFDEM®Project and was first released in 2010 in connection with the CFDEMcoupling package. The LIGGGHTS code is mainly based on the LAMMPS code of the Sandia National Labs and Temple University. It enables the calculations of inter–particle forces and heat transfer.

The simulation software contains different models, e.g. HERTZ or HOOKS, to describe granular behaviour within itself and with its surroundings as for example strain on walls. Additionally, it is able to analyse solids regarding their internal structures and behaviour to inflicted stresses [15].

Due to its open source nature the LIGGGHTS coding is easily accessible and the various methods can be extended or improved with user defined functions.

A drawback of DEM simulations and LIGGGHTS is the high demand in computational capacities, as each particle is displayed and calculated which leads to high computing times.

---

[1]Large–scale Atomic/Molecular Massively Parallel Simulator

4 Simulation Set-Up

Whereas the previous chapter formed the basic modelling for the investigated problem and has introduced adequate tools for solving it, this chapter will provide the framework of settings to implement the models into a simulation. This includes the pre–processing, e.g. the definition of the geometric model, surrounding boundary conditions to be applied and at last the solving process.

4.1 Model Dimensions

To successfully couple CFD with DEM simulation a model must be created which consists of two sub–models: One model covers the CFD simulation box, while the other covers the DEM simulation box. Both models are then merged to the CFD–DEM coupled model.
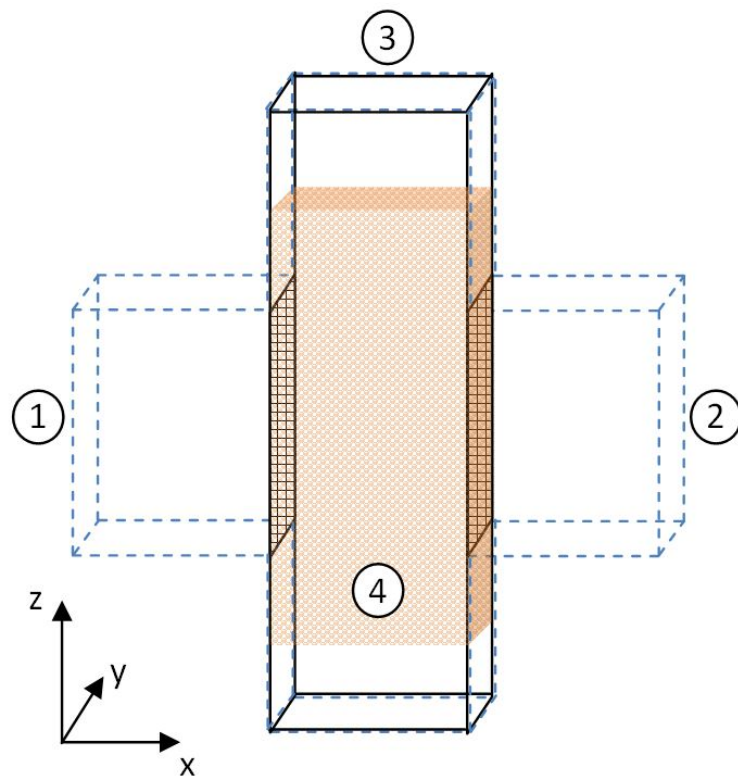
Fig. 4.1: Schematic of the quasi 2D model. ① indicates the air duct inlet, ② the air duct outlet, ③ the sand duct and ④ the sand column. Black outlines indicate the DEM, and blue dashed lines the CFD simulation box. Hatched area indicates open border between both boxes.

Figure 4.1 (p. 20) depicts the merged model based on the *VA3* heat exchanger (see Fig. 1.1, p. 2). The merged model fully encompasses the air and sand ducts, where the black outlines indicate the DEM and the blue dashed lines the CFD simulation box. For this model the CFD simulation box fully surrounds the DEM simulation box to enable fluid flow along the sand duct.

Due to the limited calculating capacity the simulations are not carried out with a 3D, but with a quasi 2D model to save computing time. For this a single slice in y–direction (depth) of the heat exchanger set–up was created.

The quasi 2D model is based on the set–up of Fig. 1.1 (p. 2), consisting of two perpendicular crossing ducts, but with a modified depth of $de_{hxz} = 2.5d_k$ to ensure that at no point in time a single particle simultaneously touches the front and back boundary. In addition, this depth allows the full development of particle–particle and fluid–particle interactions. Table 4.1 provides an overview of the respective dimensions of the heat exchange zone (hxz) for the 3D and quasi 2D models.

Tab. 4.1: Overview of model dimensions of the heat exchange zone (hxz) for 3D and quasi 2D models

		3D Model	Quasi 2D Model
Particle diameter (mm)	d_k	2.228	2.228
Hight of hxz (m)	h_{hxz}	0.14	0.14
Width of hxz (m)	w_{hxz}	0.046	0.046
Depth of hxz (m)	de_{hxz}	0.043	0.00557
Reduction factor (−)	f_{red}	1	7.72

For the heat transfer simulations a smaller model is used to investigate the impacts that granular flow effects have on the efficiency of the heat transfer. This is done to further reduce computing time while still obtaining adequate results. The heat exchange zone for the heat transfer simulations is reduced to $0.05\,\mathrm{m}$ in height and $0.02\,\mathrm{m}$ in width and depth. Particle diameter and therefore quasi 2D depth remain unchanged, resulting in the reduction factor of $f_{red.th} = 3.59$. This course of action is acceptable as Pilcher and Bridgwater [22] state that affecting pressure gradients do not depend on the geometry's dimensions but on the particles' properties [cf. 22, p. 2540].

4.2 CFD – Model

4.2.1 CFD Boundary Conditions

The CFD simulation box must encase the complete fluid region, including the sand duct as the fluid also flows between the particles. It is expanded beyond the heat exchange zone and includes the ducts to recreate any effects the ducts have on the flow development.

The CFD simulation box is meshed by simply using the *blockMesh* utility based on a *blockMeshDict* file (see [8, chapter 5.3]). Due to the basic geometric design no CAD parts are used, instead the form and patches are created manually (see Listing A.1 for the *blockMeshDict*).

For a quasi 2D model simulation the boundary conditions for the front and back (see Fig. 4.1, p. 20) of the CFD simulation box are set to *type empty* to indicate that the simulation is not solved for this dimension, assuming that each layer in this dimension shows the same behaviour. For the simulation at hand it is important to analyse the interactions of the internal sand body in this dimension and not its borders to the walls. In addition, the sand inlet and outlet are set to *type slip* to create a boundary open to the surroundings. The air inlet and outlet are set to *type patch*, while the remaining surfaces are set to *type wall*. The types *patch* and *wall* receive their respective values in the 0 folder of the CFD case. [8, chapter 5.3]

4.2.2 CFD Settings

After having set up the model for the CFD simulation different cases must be defined for the analysis stated in "2 Scope of Work". On the CFD side three cases are distinguished:

① Simulation validation with ERGUN EQUATION

② Analysis of blistering and pinning based on values provided by experimental work

③ Heat transfer analysis (exergetic efficiency)

For case ① seven simulations are set–up. The relevant settings are found in Tab. 4.2 (p. 23). The validation simulations are conducted for room temperature ($25\,°\text{C}$) and corresponding properties of air, such as the density ρ_f and the dynamic viscosity η_f, and with a sand mass flow of $\dot{m}_p = 0\,\text{g\,s}^{-1}$, as the ERGUN EQUATION describes the pressure loss along a non–moving packed bed. Therefore, a sand mass flow of $\dot{m}_p = 0\,\text{g\,s}^{-1}$ for simulation and experiment leads to a high comparability to the ERGUN EQUATION and allows for a simple validation of the simulation over the pressure gradient. The measured

values for the superficial velocities u_{free} are corrected to modified superficial velocities u_{mod}, which are used for the simulation. This modification process which depends on the geometric form is explained in A.2.

Tab. 4.2: CFD-settings for *VA3* quasi 2D simulation validation with the ERGUN EQUATION (no particle mass flow and no heat transfer)

u_{free} measured $\mathrm{m\,s^{-1}}$	u_{free} modified $\mathrm{m\,s^{-1}}$	$\dot{m}_p$ measured $\mathrm{g\,s^{-1}}$	T K	ρ_f $\mathrm{kg\,m^{-3}}$	η_f $\mathrm{kg\,m^{-1}\,s^{-1}}$
0.5	0.579				
0.75	0.868				
1.0	1.157				
1.25	1.446	0	298.15	1.184[1]	1.85e-005[1]
1.5	1.736				
1.75	2.025				
2.0	2.314				

[1] [17, Tab. A8]

The settings for case ② are stated in Tab. 4.3. The same basic conditions as for case ① apply, except for the sand mass flow. For case ② selected superficial velocities are analysed for the sand mass flows $\dot{m}_p = 18\,\mathrm{g\,s^{-1}}$ and $\dot{m}_p = 36\,\mathrm{g\,s^{-1}}$ and the related pinning and blistering effects. The first four settings for each mass flow are to determine the formation of these effects depending on the pressure difference and sand mass flow, whereas the last settings simulate equal air and sand mass flow. For the quasi 2D simulations the mass flows are adapted to the new dimensions by applying the reduction factor f_{red} (see Tab. 4.1). This leads to a simulated sand mass flows of $\dot{m}_p = 2.33\,\mathrm{g\,s^{-1}}$ ($18\,\mathrm{g\,s^{-1}}$) and $\dot{m}_p = 4.66\,\mathrm{g\,s^{-1}}$ ($36\,\mathrm{g\,s^{-1}}$).

Tab. 4.3: CFD-settings for *VA3* quasi 2D simulation of pinning and blistering with set particle mass flow and varying fluid velocities, and with equal particle and fluid mass flow (bottom two lines) (no heat transfer)

u_{free} measured $\mathrm{m\,s^{-1}}$	u_{free} modified $\mathrm{m\,s^{-1}}$	$\dot{m}_p$ measured $\mathrm{g\,s^{-1}}$	$\dot{m}_p$ adapted $\mathrm{g\,s^{-1}}$	T K	ρ_f $\mathrm{kg\,m^{-3}}$	η_f $\mathrm{kg\,m^{-1}\,s^{-1}}$
0.75	0.868					
1.0	1.157	18 / 36	2.33 / 4.66	298.15	1.184[1]	1.85e-05[1]
1.25	1.446					
1.5	1.736					
2.525	2.921	18	2.33	298.15	1.184[1]	1.85e-05[1]
5.05	5.843	36	4.66			

[1] [17, Tab. A8]

In case ③ the simulations analyse the effect blistering and pinning have on the heat transfer and therefore the exergetic efficiency of the heat exchanger. As there are no measured values available for heat transfer in the *VA3* heat exchanger and computational

time does not allow for simulating a larger heat exchanger design (*VA4*), a qualitative analysis of heat transfer and efficiency is conducted. The settings for these simulations are given in Tab. 4.4 (p. 24). As simplification the temperature dependence of the fluid properties is neglected.

For cases ① and ② the real time of the simulations is set to 5 s. After this time all simulations are converged (residuals below 0.0001) and the pressure difference follows a stable mean value with standard deviation. The case ③ simulations on the other hand have higher real time settings. The real time setting depends on the particle mass flow and is to ensure that a complete run of the particle column through the heat exchange zone carried out and stationary heat transfer is reached. For this the simulation has to meet the same criteria as the before mentioned cases with the addition that the fluid outlet temperature must also reach a stable mean value with standard deviation.

Tab. 4.4: CFD-settings for THERMO quasi 2D simulation of simple heat transfer (constant fluid properties): Case settings (top) and fluid properties (bottom); properties averaged over temperature range of 473.15 K to 1073.15 K

u_{free} measured $\mathrm{m\,s^{-1}}$	u_{free} modified $\mathrm{m\,s^{-1}}$	$\dot{m}_p$ measured $\mathrm{g\,s^{-1}}$	$\dot{m}_p$ adapted $\mathrm{g\,s^{-1}}$
3.723	4.1736	2	0.557
7.446	8.3472	4	1.114

T K	ρ_f $\mathrm{kg\,m^{-3}}$	η_f $\mathrm{kg\,m^{-1}\,s^{-1}}$	λ_f $\mathrm{W\,m^{-1}\,K^{-1}}$	c_{pf} $\mathrm{J\,kg^{-1}\,K^{-1}}$
1073.15	0.53719[1]	3.59e-05[1]	0.0541[1]	1091.02[1]

[1] [cf. 17, Tab. A8]

4.3 DEM − Model

4.3.1 DEM Boundary Conditions

The DEM simulation box must encase the (expected) granular region and loaded CAD parts. The CAD parts of the quasi 2D heat exchanger model are loaded into the simulation box to imitate the sand duct form and the particle–wall interactions. They are patched accordingly as walls and as particle inlet area. Generally the LIGGGHTS code provides a method to simulate constant particle mass flow, but it does not suffice for the problem at hand. The simulation of the Air–Sand Heat Exchanger needs a packed bed with vertical movement. To be able to simulate this packed sand column an additional CAD part is loaded as a *stopper* at the bottom of the sand column and an initial simulation for the

sand column under static conditions is performed. For the later simulations the *stopper* is used to mimic sand mass flow by applying a vertical movement. This is possible as the particle mass flow is not dependent on the depth of the particle bed [cf. 24, p. 284].

The CAD parts consist of the side parts of the sand duct, enabling to set the front and back boundaries to *periodic (p)*. This leads to particles leaving the simulation box at the front to re-enter at the back and vice versa. Therefore, the particle interaction of a particle bed with greater depth can be simulated without the need of a 3D model. It is important to note that this approach also eliminates wall effects that otherwise would occur, which leads to inaccuracies of the simulation if these effects have a high impact in the 3D model [cf. 3, p. 666]. Listings A.2 and A.3 show the DEM simulation codes.

4.3.2 DEM Settings

With the three cases specified in "4.2.2 CFD Settings" two different settings are needed for the DEM simulation. The first settings are given in Tab. 4.5 for different sand mass flows but without heat transfer.

For DEM simulation the mechanical properties of the material is of very high importance as they dictate the particle–particle and particle–wall interactions. As the material properties for quartz are not known these are taken from other sources as stated when applicable.

The particle size distribution of 1 mm - 2 mm with a Sauter particle diameter of 1.63 mm, as used in the experiments, is too small and results in very high computing times with the limited computational capacity available. Therefore, a larger particle size distribution of 2 mm - 3.15 mm is chosen for the simulations, which is still within the range of usable sand sizes. The Sauter diameter derived for this particle size distribution is 2.228 mm. The process of deriving the Sauter diameter from a particle size distribution is explained in A.1.

According to Schulze [25] the two major factors for particle flow are the particle size and the adhesive force [cf. 25, chap. 2]. The adhesive forces are implemented to the DEM code by stating the friction coefficients. As Tab. 4.5 indicates these values are not known for the experimental set–up. Therefore, a sensitivity analysis (SA) covering these factors is carried out, based on the settings of Tab. 4.5 (p. 26).

The fluid velocity and particle mass flow are unchanged for each simulation. The chosen values of $2.5 \, \text{m s}^{-1}$ and $18 \, \text{g s}^{-1}$ correspond to equal mass flows of the fluid and particles. This setting provides defined pinning and blistering behaviour which form the basis for

Tab. 4.5: DEM-settings for different particle mass flows (no heat transfer)

		0 g s^{-1}	**18 g s^{-1}**	**36 g s^{-1}**
Particle diameter (mm)	d_k		2.228	
Adapted mass flow (g s^{-1})	$\dot{m}_p$	0	2.33	4.66
Stopper velocity (m s^{-1})	u_p	0	5.68e-03	11.37e-03
Young's Modulus (Pa)	E_p		74e07[3]	
Poisson Ratio (−)	ν_p		0.12[3]	
Friction coeff. (particle–particle) (−)	f_{pp}		0.7[1]	
Friction coeff. (particle–wall) (−)	f_{wp}		0.8[2]	
Restitution coeff. (particle–particle) (−)	k_{pp}		0.7[1]	
Restitution coeff. (particle–wall) (−)	k_{wp}		0.8[4]	
Particle temperature (K)	T		298.15	

[1] [34, Tab. 1]; [2] [14, Tab. 13]; [3] [16, p. 301]; [4] estimated value

the sensitivity analysis. Within the SA various friction coefficients for particle–particle (p–p) and wall–particle (w–p) friction are applied (see Tab. 4.6).

As the particle size for the simulations is only marginally larger than the experimental size, the SA does not incorporate the effects of changing particle sizes.

Tab. 4.6: Overview of changed friction coefficients (red) for sensitivity analysis

	u_{free}	$\dot{m}_p$	friction coefficient	
	m s^{-1}	g s^{-1}	p–p −	w–p −
low friction			0.7	0.4
high friction	2.5	18	0.7	1.6
low internal friction			0.35	0.8
high internal friction			1.4	0.8

The second collection of settings is for the heat transfer simulation. For this the DEM settings are similar to the CFD settings. To be able to compare the simulation results with analytical solutions, the particle properties which are in fact temperature dependent are set to constant values, which are averaged over the investigated temperature range. The applied particle properties for the heat transfer simulation are stated in Tab. 4.7.

Tab. 4.7: DEM-settings for THERMO quasi 2D simulation of simple heat transfer (constant particle properties) as extension of Tab. 4.5; thermal properties averaged over temperature range of 473.15 K to 1073.15 K

		2 g s^{-1}	**4 g s^{-1}**
Adapted mass flow (g s^{-1})	$\dot{m}_p$	0.557	1.114
Stopper velocity (m s^{-1})	u_p	3.125e-03	6.25e-03
Particle temperature (K)	T		473.15
Thermal conduction (W m^{-1} K^{-1})	λ_p		5.8565[1]
Heat capacity (J kg^{-1} K^{-1})	c_{pp}		1050[2]

[1] [32, Fig. 4]; [2] [10, Tab. 3]

The temperature distribution within the particles are assumed to be uniform. This is acceptable, when the BIOT NUMBER, which sets the conduction ability of the particle into relation with the surface heat transfer, Bi is [cf. 23, p. 97]

$$Bi = \frac{\alpha L}{\lambda} \ll 1. \tag{4.1}$$

For the conducted simulations this requirement is fulfilled with $Bi = 0.24$ for the first and $Bi = 0.33$ for the second thermal simulation.

For all simulation cases a general DEM setting is carried out to better visualise the particle flow behaviour. All particles are divided into differently coloured groups based on their identification number. This grouping initially leads to differently coloured horizontal particle layers in the particle column. The respective particles retain their colouring throughout the simulations, therefore the movement of the particles within the particle mass flow can be followed.

4.4 CFDEMcoupling – Merging the Models

In the previous sections the parameters for CFD and DEM simulations were set. To enable the coupling of both simulations further parameter settings must be performed.

The CFDEMcoupling has a significant influence on the specification of the time steps. It connects the DEM simulation with the CFD simulation via the *couplingInterval* command. This command must be set to accommodate the requirements stated by the COURANT–FRIEDRICHS–LEVY Condition and the RAYLEIGH TIME. Typically the coupling interval ranges from $50 - 100$ time steps [cf. 27, p. 5], depending on the application. The process to determine the time steps and the coupling interval is to first calculate the RAYLEIGH TIME, then set the percentage which is to be the DEM time step. Secondly the coupling interval must be specified. This depends greatly on the simulated aspect, simple models allow higher intervals, whereas more complex models require low intervals to solve correctly. The last step is to derive the CFD time step from the connected DEM time step and coupling interval. In addition the resulting CFL number is checked regarding pre–set criteria. If the CFL number should not meet the criteria the coupling interval has to be reduced until the COURANT–FRIEDRICHS–LEVY Condition is fulfilled.

For all simulations the CFL number is to be $c_{max} \leq 1$ and the DEM time step $10\,\%$ of the RAYLEIGH TIME. The coupling interval was set according to the nature of the conducted simulation. A high coupling interval decreases the computing time, but it also reduces

the number of updates of, for example, the momentum exchange between DEM and CFD. The resulting parameters are shown in Tab. 4.8.

Tab. 4.8: CFDEM-settings for fluid-particle interaction simulation and thermal simulation

		fluid-particle	thermal (1)	thermal (2)
Rayleigh Time (s)	Δt_R		1.1e-05	
Time step portion (%)	-		10	
DEM time step (s)	Δt_{DEM}		1.0e-06	
Coupling interval $(-)$	-	100	100	10
CFD time step (s)	Δt_{CFL}	1.0e-04	1.0e-04	1.0e-05
Simulation mesh cell width (m)	Δx		0.005	
highest fluid velocity $(\mathrm{m\,s^{-1}})$	u_{mod}	2.921	4.1736	8.3472
CFL number $(-)$	c	0.0584	0.0835	0.0167

The rounded off value for the DEM time step is chosen to simplify the conversions of output intervals between the DEM and CFD simulations. Regarding the CFD number it is to note that in Tab. 4.8 it may appear that a larger time step on the CFD side could be chosen, as the CFL number determined is significantly smaller than 1. Nevertheless, in the CFDEMcoupled simulation the CFL number is highly dependent on the particle flow and varies throughout the simulation. These small values ensure that the simulation is stable for all fluid velocities investigated.

Next to the time step control the CFDEMcoupling observes the heat transfer from fluid to particle and vice versa. For this the remaining thermal fluid properties are implemented. These are shown in Tab. 4.4 (p. 24) in section "4.2.2 CFD Settings".

5 Results

The following sections show the results of the numerical and analytical investigations which were conducted for the Air–Sand Heat Exchanger. The main focus hereby lies on the granular flow effects induced by high fluid velocities and their additional effect on the heat transfer between fluid and particles.

5.1 Validation of Simulation Set–Up

During experiments with the *VA3* prototype and sand of the size distribution of $1\,\mathrm{mm}$ to $2\,\mathrm{mm}$ Niederwestberg [21] found that the pressure drop along the sand column for a sand mass flow of $\dot{m}_p = 0\,\mathrm{g\,s^{-1}}$ correlated with the ERGUN EQUATION for non–moving beds [cf. 21, p. 75]. Figure 5.1 shows the correlation between the measured pressure gradient (red) and the solved ERGUN EQUATION (green) with expected and acceptable marginal deviations.
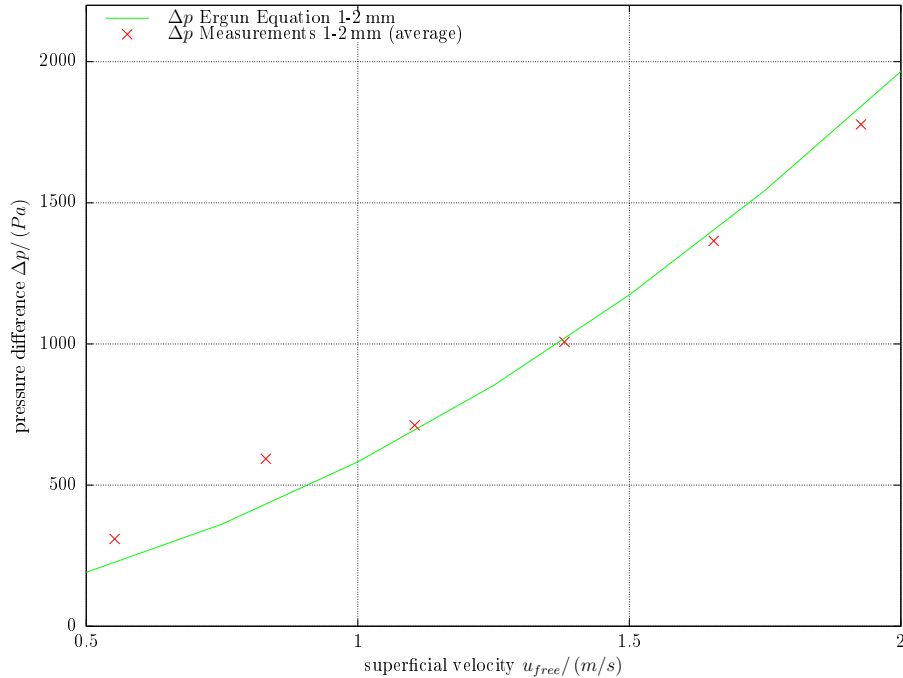
Fig. 5.1: Comparison of the pressure difference Δp over the superficial velocity u_{free} as the analytical results of the Ergun Equation (green) and laboratory measurements (red) for particle diameter $d_p = 1.63\,\mathrm{mm}$ [cf. 21, p. 75]

Based on this observation the ERGUN EQUATION is used to validate the simulation with a particle size distribution of $2\,\mathrm{mm}$ to $3.15\,\mathrm{mm}$ and a sand mass flow of $\dot{m}_p = 0\,\mathrm{g\,s^{-1}}$. Also

it is assumed that the differences in pressure gradient development are negligible as the change in diameter is insignificant (a comparison of Ergun solutions for both diameters can be seen in Fig. 5.3, p. 31). The settings used for the simulations are stated in Tab. 4.2 (p. 23).

In Fig. 5.2 the simulation shows the same behaviour as the measurements, for small velocities the pressure gradient is slightly larger than the analytical solution, whereas it is smaller for higher velocities.
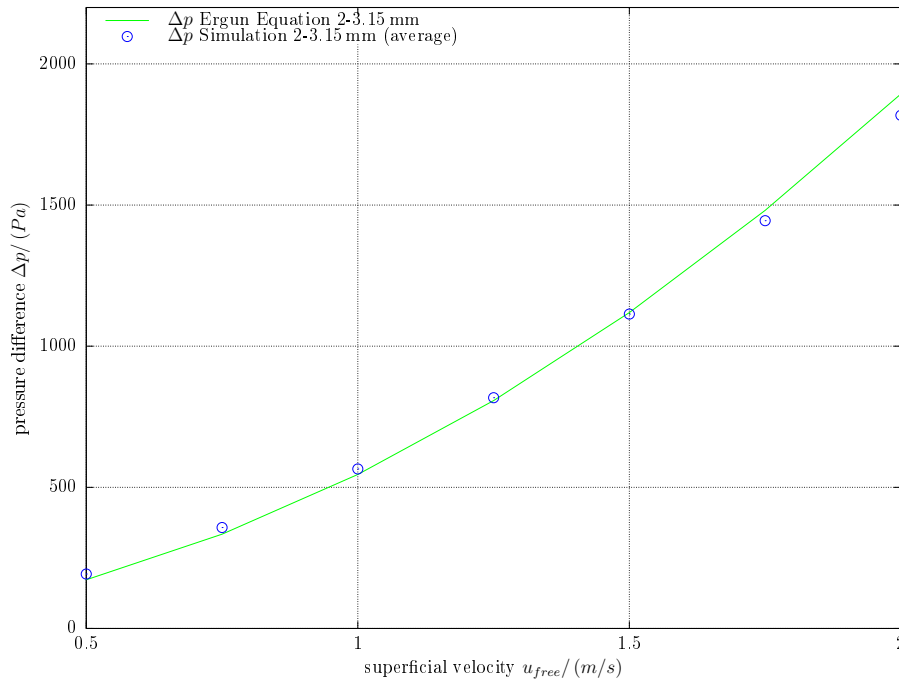
Fig. 5.2: Validation of simulation results based on pressure difference Δp over superficial velocity u_{free}; comparison of Ergun Equation results (green) and simulation results (blue) particle diameter $d_p = 2.228\,\mathrm{mm}$

Together Figures 5.1 and 5.2 demonstrate that the coupled CFD–DEM simulation is capable of solving the fluid flow behaviour through bulk solids according to the experimental observations.

In addition, the pressure gradients for a sand mass flow of $\dot{m}_p = 18\,\mathrm{g\,s^{-1}}$ are compared with the ERGUN EQUATION solutions. This is done for the measurements with $d_p = 1.63\,\mathrm{mm}$ sand diameter and for the simulations with $d_p = 2.228\,\mathrm{mm}$. Figure 5.3 (p. 31) depicts the outcome of this comparison. Interestingly, the red graph indicating the measured data differs greatly from the analytically expected solution. The measured data is significantly higher and the deviation increases with higher velocities. In contrast to this, the simulated data follows the analytical solution for the most part. Only for high velocities does the simulated pressure gradient fall below the Ergun solution. Nevertheless, the simulations

correlate to the observations made by CHEN et al. [6]. In their study CHEN et al. [6] found that the fluid flow impacted the particle flow in such a way that the packing situation changed, for example a cavity was created and therefore the pressure gradient decreased [cf. 6, p. 188].
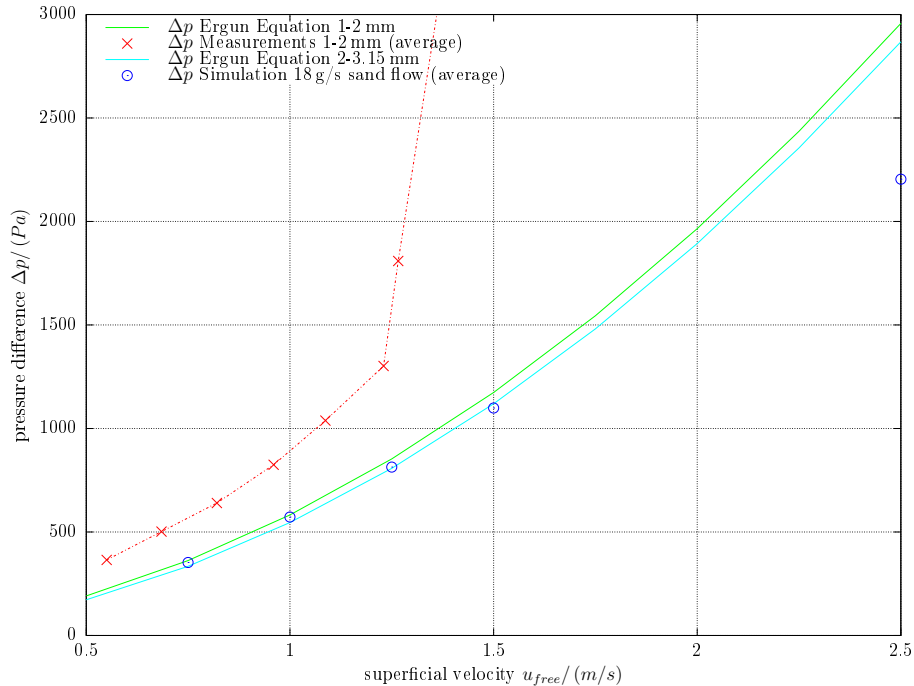
Fig. 5.3: Comparison of pressure difference Δp over superficial velocity u_{free} as results of the Ergun Equation for measured values (green and red) and simulation results (cyan and blue). The measured and simulated values are for a sand mass flow of $18\mathrm{g\,s}^{-1}$.

The measured pressure gradient on the other hand is assumed to increase due to the high portion of fine particles contained in the sand. While the simulation operates with a single diameter for all particles, the experiment contains a certain range of particle sizes which are grinded into even smaller particles during operation. During the movement of the particle bed it is assumed that the fine particles are carried along forming cavities through the sand column, and then clog the separating grid, thus increasing the pressure gradient. This process can be compared to the segregation of mixed particles [cf. 24, p. 294].

The used model does not include the separating grid as itself does not have a significant impact on the pressure gradient. To further investigate the observed phenomenon of increased pressure gradient for sand mass flow, a simulation incorporating a set particle size distribution (including a high portion of fine particles) and a CAD part of the separating grid, as well as high computational capacities would be required.

5.2 Granular Flow Effects

The next step in analysing the usefulness of the CFD–DEM simulation to describe flow effects is to compare the measured points of effect initialisation with simulated data.

In contradiction to Pilcher and Bridgwater [cf. 22, p. 2539] Niederwestberg [21] observed in his experiments that the pinning effect was initialised prior to the blistering effect. The measured pressure gradient for the beginning of pinning is 368 Pa, whereas for blistering it is 811 Pa [cf. 21, p. 71]. As the only change between the experiments and simulations is a slight increase of particle diameter, it is assumed that the simulation should show the flow effects at marginally higher pressure gradients. Therefore, the simulations are carried out for the settings specified in Tab. 4.3 (p. 23), as these cover the expected range of pressure gradients.

In Fig. 5.4 (p. 5.4) the simulated fluid velocity dependent particle flows are provided. Simulation ① shows that the set–up of the heat exchanger enables a mass flow, as the particle layers form a distinct u–shaped velocity profile. In simulation ③ it can be seen that the pinning sets in on the fluid outlet side—as indicated by the orange dashed line— at a pressure gradient of between 352.46 Pa and 572.10 Pa. It is notable that the pinning is more dominant at the top of the heat exchange zone than at the bottom. With increasing fluid velocity and pressure gradient the particle velocity profile continues to change, as demonstrated in ④. The pinning slightly increases, and in addition the u–shape on the fluid inlet side dissolves, indicating that the velocity of the particles at the fluid's inlet is higher than at the fluid's outlet, confirming the increase in pinning. The next step is shown in ⑤, where the blistering process begins at between 813.33 Pa and 1098.74 Pa.

Similar observations can be made for the simulations with a sand mass flow of $36\,\mathrm{g\,s^{-1}}$, except that the characteristics of the flow effects are more dominant than for a particle mass flow of $18\,\mathrm{g\,s^{-1}}$. But this is generally incited by the different particle velocities induced by the set mass flow. The presentation and comparison of $36\,\mathrm{g\,s^{-1}}$ particle mass flow at varying fluid velocities can be found in Fig. 5.5 (p. 34).

Overall the CFD–DEM simulation is able to reproduce the observed effects the fluid flow has on the particle flow at higher fluid velocities. Nevertheless, the intensity of the effects differs from the experimental observations. During the experiments the pinning effect would lead to a complete halt of the sand layers directly at the separating mesh, the layer thickness increasing with higher fluid velocities. The simulations on the other hand only show a deceleration of these particles, only at very high fluid velocities do these particles stagnate. This phenomenon is further investigated in "5.3 Sensitivity Analysis".
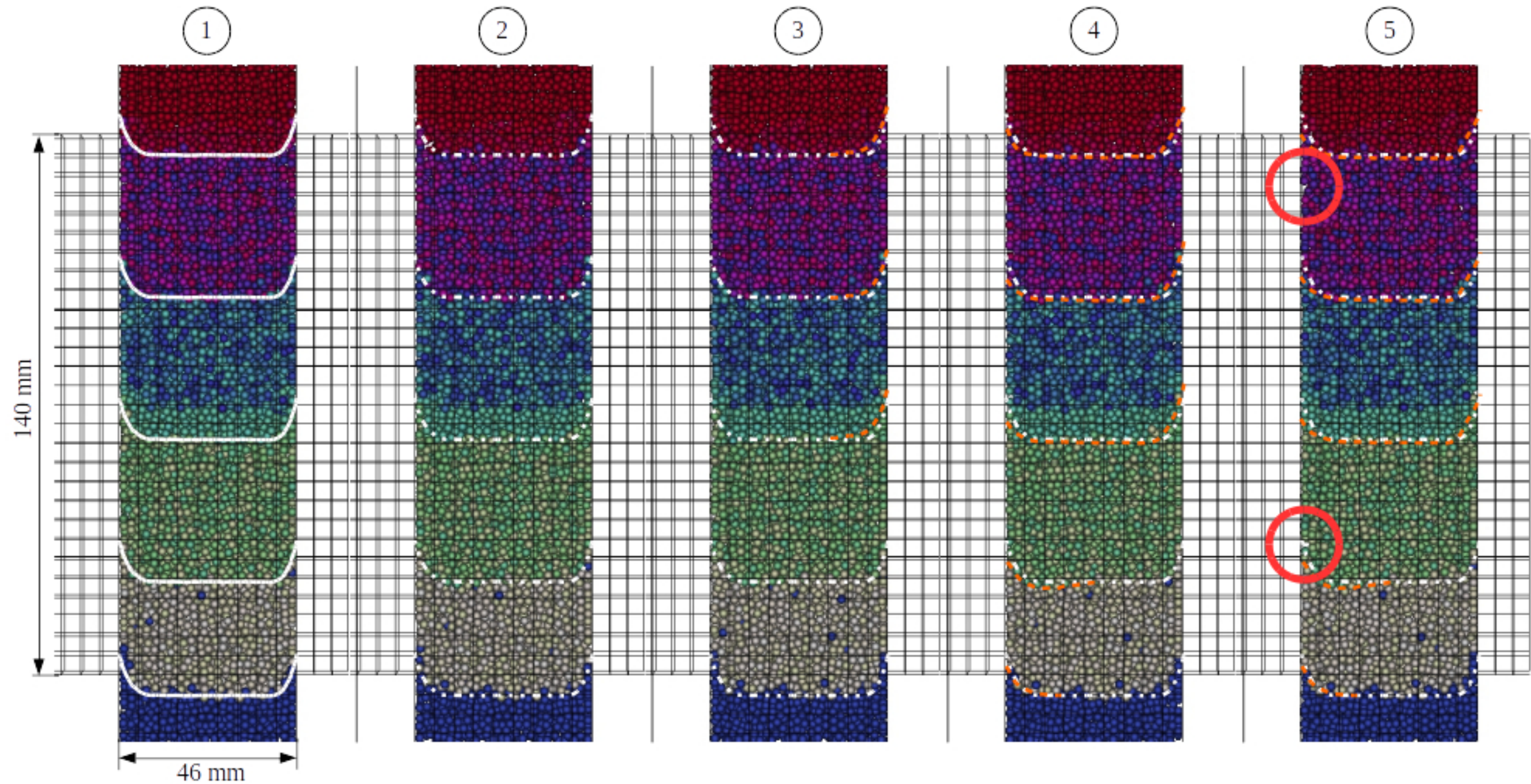
Fig. 5.4: Comparison of constant particle flow $(18\,\mathrm{g\,s^{-1}})$ under the influence of varying fluid velocities u_{free} after 5 s real time: ① $0\,\mathrm{m\,s^{-1}}$ and $\Delta p = 0\,\mathrm{Pa}$; ② $0.75\,\mathrm{m\,s^{-1}}$ and $\Delta p = 352.46\,\mathrm{Pa}$; ③ $1.0\,\mathrm{m\,s^{-1}}$ and $\Delta p = 572.10\,\mathrm{Pa}$; ④ $1.25\,\mathrm{m\,s^{-1}}$ and $\Delta p = 813.33\,\mathrm{Pa}$; ⑤ $1.5\,\mathrm{m\,s^{-1}}$ and $\Delta p = 1098.74\,\mathrm{Pa}$. Coloured particles indicate different layers to better visualise particle movements. White dashed line indicates original layer outline from ①. Orange dashed line indicate layer changes, starting with pinning at fluid flow outlet in ③. Red circles indicate blistering. Particles flow vertically downwards, the fluid flows horizontally from left to right for each column separately. For the particle flow of $18\,\mathrm{g\,s^{-1}}$ the particles have an average retention time of 24 s in the heat exchange zone.
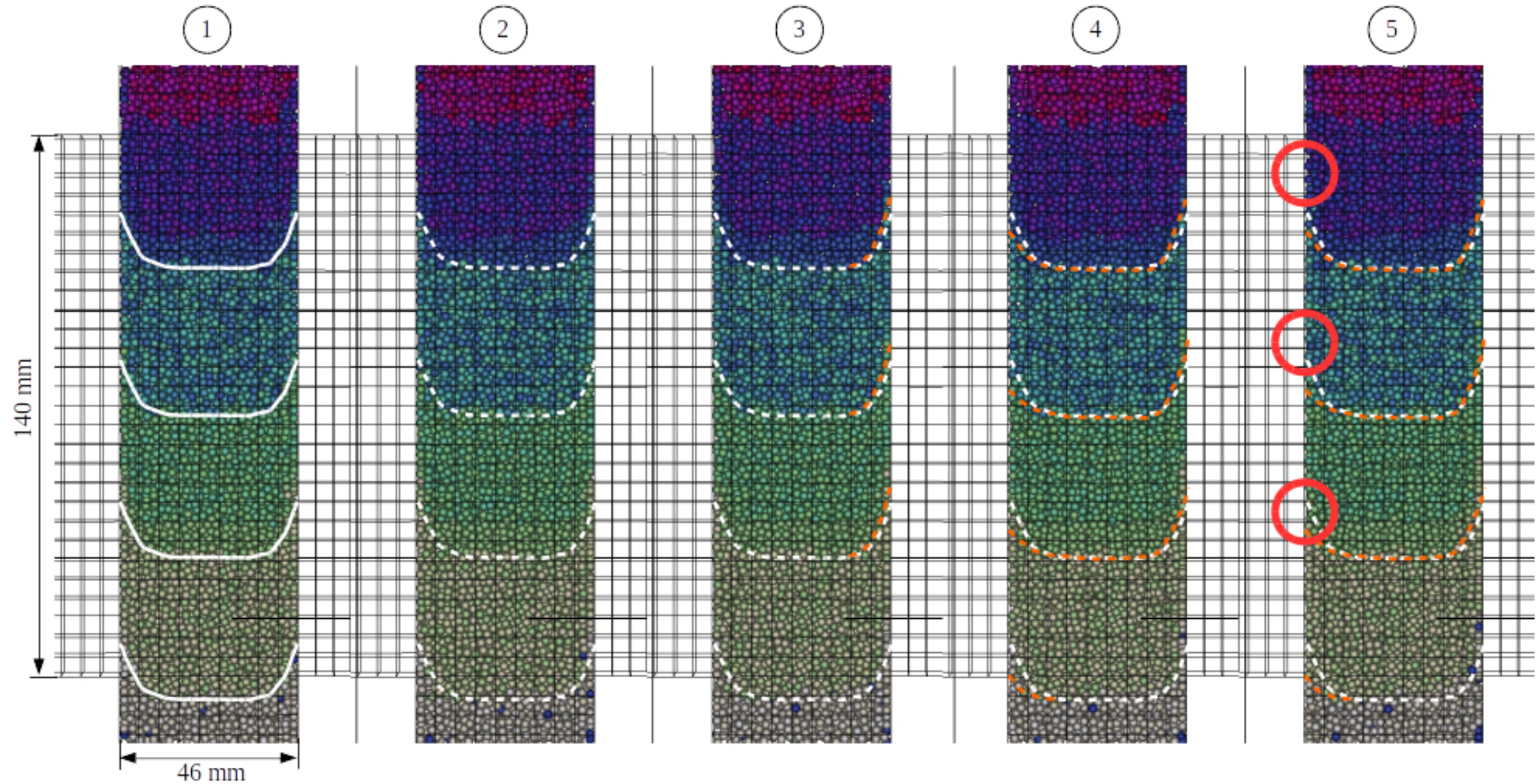
Fig. 5.5: Comparison of constant particle flow ($36\,\mathrm{g\,s^{-1}}$) under the influence of varying fluid velocities u_{free} after $5\,\mathrm{s}$ real time: ① $0\,\mathrm{m\,s^{-1}}$ and $\Delta p = 0\,\mathrm{Pa}$; ② $0.75\,\mathrm{m\,s^{-1}}$ and $\Delta p = 351.72\,\mathrm{Pa}$; ③ $1.0\,\mathrm{m\,s^{-1}}$ and $\Delta p = 557.62\,\mathrm{Pa}$; ④ $1.25\,\mathrm{m\,s^{-1}}$ and $\Delta p = 809.97\,\mathrm{Pa}$; ⑤ $1.5\,\mathrm{m\,s^{-1}}$ and $\Delta p = 1086.81\,\mathrm{Pa}$. Coloured particles indicate different layers to better visualise particle movements. White dashed line indicates original layer outline from ①. Orange dashed line indicate layer changes, starting with pinning at fluid flow outlet in ③. Red circles indicate blistering. Particles flow vertically downwards, the fluid flows horizontally from left to right for each column separately. For the particle flow of $36\,\mathrm{g\,s^{-1}}$ the particles have an average retention time of $12\,\mathrm{s}$ in the heat exchange zone.

A depiction of granular flow effects with dominant pinning,blistering and blocking behaviour is shown in Fig. 5.6. The left segment shows the distinct form of the *filter cake* caused by the pinning effect, which matches the schematic outlines in "3.1 Definitions". In addition, the deformation of the particle layers caused by the pinning and blistering effect and the accompanying acceleration of particle flow to compensate the loss in cross section is visible. The right segment shows a fully developed case of blocking. The particle layers are unchanged, no particle mass flow has taken place.
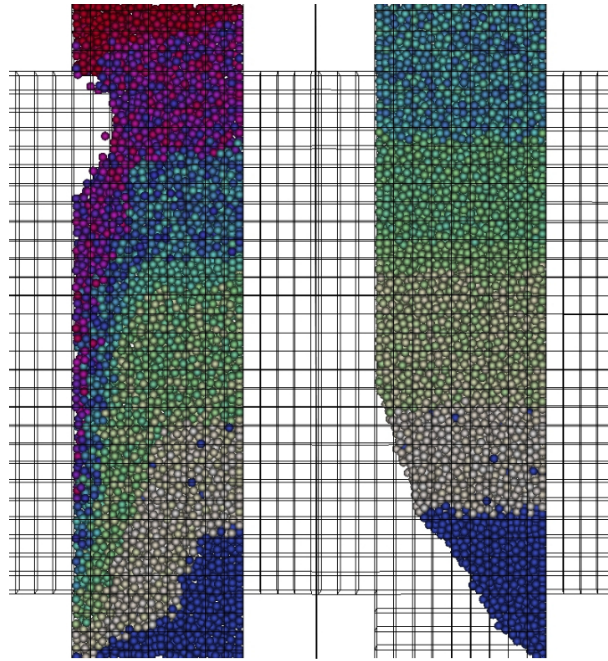
Fig. 5.6: Particle layer deformation caused by distinct pinning and blistering effects (left, for $\dot{m}_p = \dot{m}_f = 18\,\mathrm{g\,s^{-1}}$) and unchanged particle layers due to blocking (right, for $\dot{m}_p = \dot{m}_f = 36\,\mathrm{g\,s^{-1}}$).

The granular flow effects are equally visible in the void fraction of the bulk solids. Figure 5.7 (p. 36) shows the void fraction over the height of the heat exchange zone at $0.01\,\mathrm{m}$ and $0.036\,\mathrm{m}$ of the zone's width. For a mass flow of $18\,\mathrm{g\,s^{-1}}$ the void fractions on the air inlet side are considerably higher than the averaged void fraction for this particle mass flow without any effects of 0.4. The void fractions on the outlet side are significantly below the average void fraction except for where the *filter cake* ends. It is also visible that the void fraction increases slightly on the same level blistering occurs, especially in the top section of the heat exchange zone. For a mass flow of $36\,\mathrm{g\,s^{-1}}$ these observations cannot be made. The void fractions on in- and outlet side lie significantly below average and are relatively close to each other in their trend. The only difference is seen for the bottom section of the heat exchange zone for which the void fraction on the inlet side nears 1, as no particles reside here.
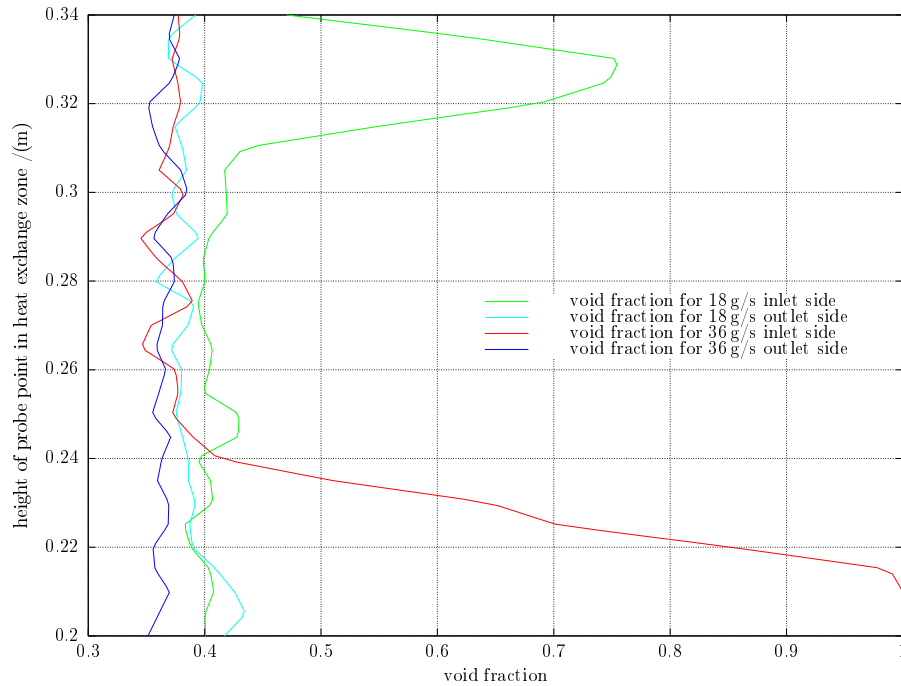
Fig. 5.7: Comparison of the void fractions for $18\,\mathrm{g\,s^{-1}}$ and $36\,\mathrm{g\,s^{-1}}$. Values taken from probe locations at heat exchanger zone widths $0.01\,\mathrm{m}$ and $0.036\,\mathrm{m}$.

From Figures 5.7, 5.4 (p. 33), 5.3 (p. 31), and the observations, made it can be concluded that whereas the simple granular mass flow retains its void fraction, the fluid mass flow has considerable impact on the packing structure of the granular material. Leading to the analysed granular flow effects and hence influencing the void fraction and the correlation of the pressure gradient with the ERGUNG EQUATION.

5.3 Sensitivity Analysis

As stated in 4.3.2 DEM Settings the friction coefficients for the quartz sand used in the experiments are not known, therefore values were assumed based on other studies. The sensitivity analysis confirms that the differences between the simulation results and the experimental findings arise from the made assumptions.

Figures 5.8 (p. 37) and 5.9 (p. 38) depict the influence the friction coefficients have on the granular flow. In both figures the middle segment displays the granular flow effects for the assumed friction coefficients, whereas the left depicts the simulation with a smaller coefficient and the right a larger coefficient.

In Fig. 5.8 the effect of the wall-particle friction coefficient is investigated. In the starting position of the sand column the deep red particle layer would not be seen. Comparing

case ① (low friction) with case ③ (high friction) it is visible that the friciton coefficient dictates the behaviour of the particles close to the outlet wall. In the first case the low friction coefficient leads to a slight deceleration of the particles. Whereas for the high friction coefficient the particles reach a complete stop and actual pinning as observed in the experiments takes place. The w-p friction only affects on the outlet side of the particle columns, as the fluid flow on the inlet side detaches the particles from the separating mesh (minor blistering).

Fig. 5.8: Comparison of the impact of the wall-particle friction on the particle flow effects for particle mass flow of $18\,\mathrm{g\,s^{-1}}$ and fluid velocity of $2.5\,\mathrm{m\,s^{-1}}$. Left low friction (Tab. 4.6, p. 26), middle standard friction (Tab. 4.5, p. 26), right high friction (Tab. 4.6, p. 26).

Comparing case ③ with the standard simulated case ② indicates that the assumed wall-particle friction coefficient of 0.8 is lower than the specific quartz property.

Figure 5.9 on the other hand depicts the effects of particle-particle friction on granular flow behaviour. Again the middle segment shows the standard simulation conducted, the left low internal friction, and the right high internal friction. Generally it can be said that the internal friction has similar impact on the granular flow behaviour as the wall–particle friction. High internal friction coefficients lead to a stop of particle movement at the walls, while small values decelerate the particles.

The most important impacts of the friction coefficients is seen when comparing p–p and w–p friction, in this instance the both cases ③ of the Fig. 5.8 and 5.9. As previously

indicated the fluid flow detaches the particles from the separating mesh on the inlet side. Therefore, it is assumed that for this comparison the wall friction on the inlet side can be neglected. This leads to the observation that the layer deformation of the simulation with standard internal friction is greater than of the simulation with high internal friction. For the standard internal friciton (Fig. 5.8, p. 37) the turquoise layer reaches below the bottom edge of the fluid inlet, although this simulation had a higher wall friction; whereas the turquoise layer in the simulation with high internal friction and standard wall friction reaches just above the bottom edge of the fluid inlet. Similar observations can be made with both ① of the friction cases.
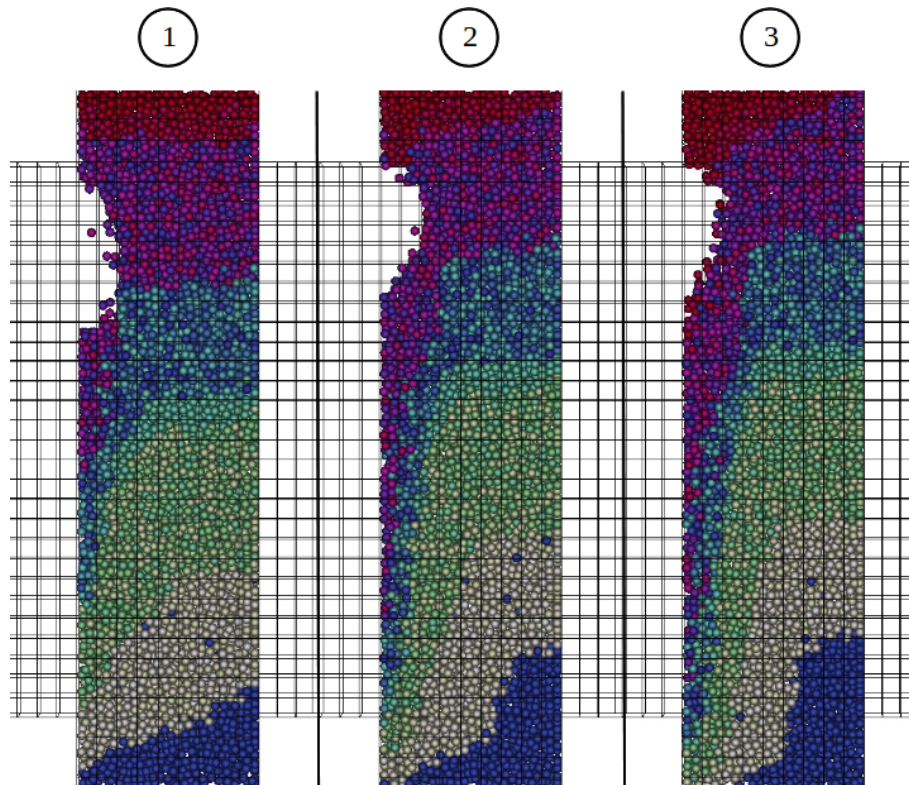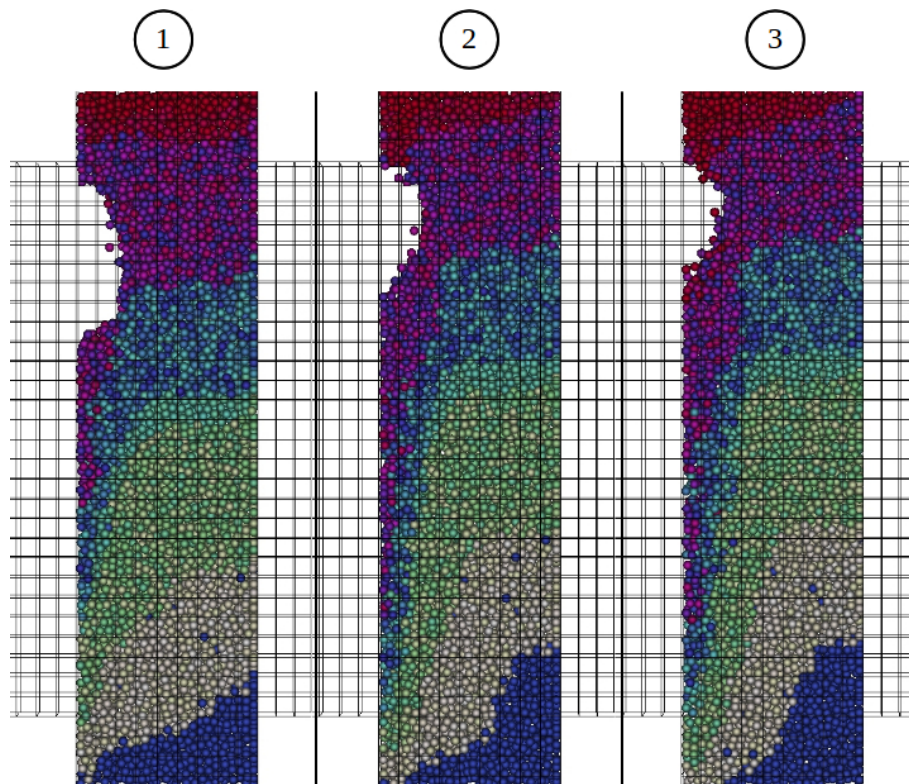

Fig. 5.9: Comparison of the impact of the particle-particle friction on the particle flow effects for particle mass flow of $18\,\mathrm{g\,s^{-1}}$ and fluid velocity of $2.5\,\mathrm{m\,s^{-1}}$. Left low friction (Tab. 4.6, p. 26), middle standard friction (Tab. 4.5, p. 26), right high friction (Tab. 4.6, p. 26).

The sensitivity analysis confirms the importance to determine the specific friction coefficients, as they strongly influence the correct display of granular flow behaviour. Whereas the w-p friction coefficient determines the grade of deceleration of the mass flow, the p-p additionally influences how far the wall friction reaches into the particle column. Also it describes the interactions (and interdependent obstructions) of the particles. These aspects are in accordance to chapter 2.6 of [25].

Overall the sensitivity analysis proves the ability of the simulation set-up to adequately simulate granular flow effects caused by the fluid's velocity and pressure gradient.

5.4 Temperature Transfer under Flow Effects

In the last step of "Scope of Work" the simulations are to be analysed regarding the heat transfer and the resulting exergetic efficiency. As stated in "4.2.2 CFD Settings" no experimental data for the heat transfer in *VA3* is available and simulating the larger set–up *VA4* leads to infeasible computing times. Therefore a smaller geometric model and the parameters from Tables 4.4 (p. 24) and 4.7 (p. 26) are used. Missing experimental data is substituted with the P–NTU METHOD, which is used to analytically determine the expected output temperatures.

The analytical solution of the P–NTU METHOD is to display the heat exchange behaviour between the fluid and the particle phase under the assumption that no granular flow effects occur (ideal case). Built up on this two thermal cases are simulated that will lead to granular flow effects. The first case $(2\,\mathrm{g\,s^{-1}})$ will contain pinning and blistering, while the second case $(2\,\mathrm{g\,s^{-1}})$ will have blocking. The respective values are found by applying the findings discussed in "5.2 Granular Flow Effects" and "4.1 Model Dimensions".
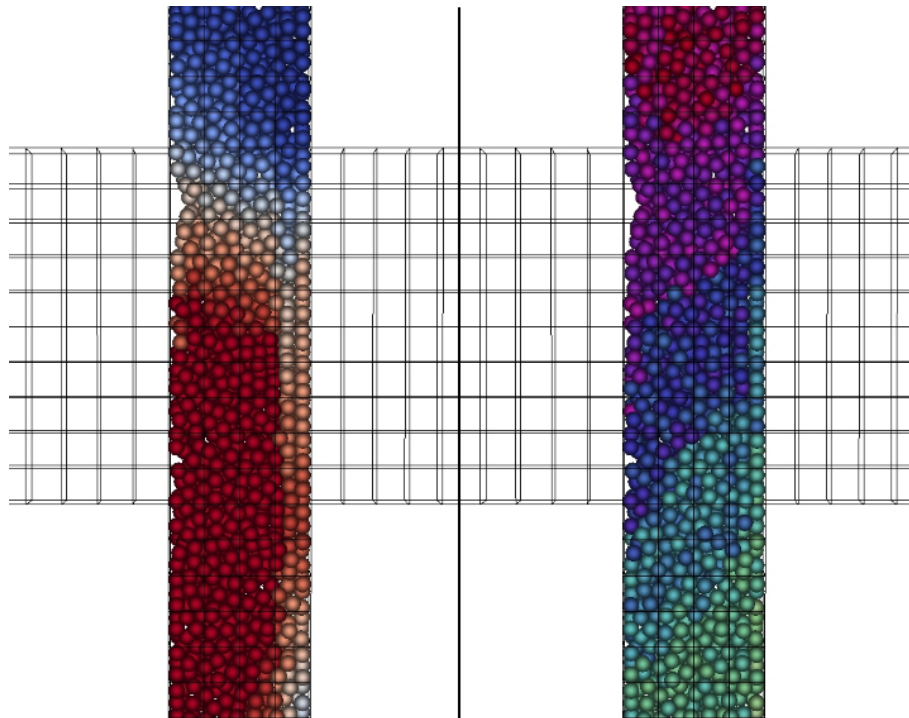
Fig. 5.10: Particle temperature distribution (hot = red; cold = blue) for granular flow with pinning and blistering effects (left) and particle layer deformation due to pinning and blistering (right) (THERMO setup)

Figure 5.10 contains the temperature distribution (left) and the layer deformation (right) for $2\,\mathrm{g\,s^{-1}}$ particle and fluid mass flow after $17\,\mathrm{s}$. In this case pinning and blistering takes place. With a cross flow and approximately equal heat capacity rates a clean temperature

distribution would be expected. At the particle inlet of the heat exchange zone the mean particle temperature is the lowest and at the outlet the highest with a linear trend in–between. Figure 5.10 (left) shows the interference granular flow effects have on the heat transfer. The differences in temperature distribution correlates strongly with the layer deformation depicted in Fig. 5.10 (right), which shows the pinning effects on the fluid outlet side and the resulting accelerated particle flow on the fluid inlet side of the heat exchanger. The pinned particles have a higher retention time, thus gaining more heat than for their location expected. This effect is slightly subdued by the accelerated (cold) particle flow on the inlet side.

A direct comparison of the expected temperature distribution within the heat exchange zone and the simulation results is given in Fig. 5.11. The simulation results provided (blue diamonds) in this figure indicate the location at which a significant temperature drop to previous temperatures takes place (5 % deviation). The red line indicates the analytically expected temperature distribution.It is clearly visible that the temperature distribution is off–set to the fluid outlet area, where pinning occurs.
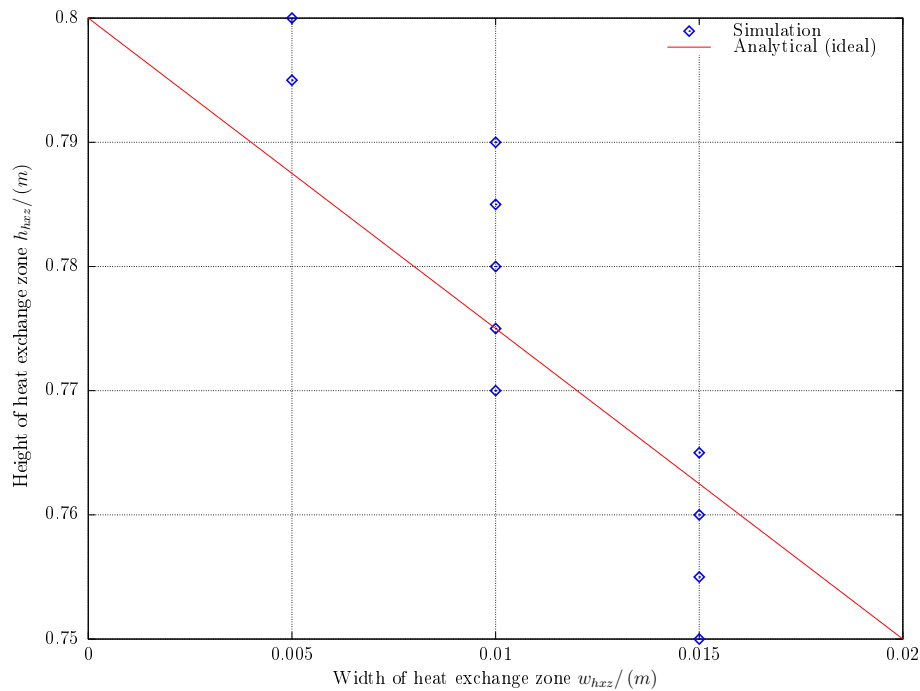
Fig. 5.11: Comparison of locations for significant drops of fluid temperature within heat exchange zone: Red line indicates the locations for ideal heat transfer; the blue diamonds indicate the simulation results (THERMO set-up) $(2\,\mathrm{g\,s^{-1}})$.

To be able to determine the exergetic efficiency of this simulation case based on "3.3.2 Exergetic Efficiency of Heat Exchanger" and to analyse the impact of granular flow effects the output temperatures of the ideal case have to be calculated analytically. For this Equations (3.7) to (3.14) (p. 9) and the P–NTU METHOD (see section 3.3.3) are used.

The particle diameter $d_k = 2.228\,\mathrm{mm}$ is applied for the characteristic length L and the void fraction of the fluid set to $\Psi = 0.4$. The full calculations are found in A.4 as Matlab code.

The resulting heat transfer coefficient is $\alpha = 636.13\,\mathrm{W\,m^{-2}\,K^{-1}}$, the dimensionless numbers $NTU = 2.6238$ and $P = 0.56329$ for the first case of thermal simulation with a mass flow of $2\,\mathrm{g\,s^{-1}}$. The simulated and analytically derived results for the particle and fluid flow outlet temperatures are provided in Tab. 5.1. It can be seen that the simulated outlet temperature for the particle flow lies $9\,\%$ beneath the analytical solution, whereas the fluid outlet temperature exceeds the analytical value by approximately $5\,\%$. Due to the hindered particle flow the heat transfer is not ideal and the achieved temperature differences are smaller than those of the ideal case. These changes in temperature differences lead to a reduction of exergetic efficiency, as it is defined as the ratio of the useful exergy and the invested exergy and the exergy depends on the operating temperature in comparison to the ambient temperature.

Tab. 5.1: Comparison of analytical and simulated output temperatures for fluid and particle flow (THERMO set-up)

	Analytical K	Simulated K	Deviation %
$T_{p.in}$	473.15	473.15	—
$T_{f.in}$	1073.15	1073.15	—
$T_{p.out}$	811.13	737.45	- 9.08
$T_{f.out}$	735.17	770.01	+ 4.74
$T_{p.in} - T_{p.out}$	- 337.98	- 264.3	—
$T_{f.in} - T_{f.out}$	337.98	303.14	—

Table 5.2 (p. 42) provides the data of the exergy efficiency analysis. It shows that the exergy flow released by the fluid in the simulations is lower than for the ideal case. At the same time the received exergy flow of the particles is significantly smaller for the simulation than for the analytical case. Although the ideal case used the ERGUN EQUATION solution for the pressure gradient, which was previously found to overestimate the pressure drop for high particle mass flows, it still reaches an exergetic efficiency of $75\,\%$, whereas the simulated heat transfer—affected by the granular flow effects pinning and blistering— reaches only $62\,\%$ efficiency.

Tab. 5.2: Overview of exergetic efficiency analysis results for analytically ideal and simulated case with $2\,\mathrm{g\,s^{-1}}$ mass flow.

	$\boldsymbol{\Delta p}$ Pa	$\boldsymbol{\kappa}$ $-$	$\dot{\boldsymbol{E}}_{\boldsymbol{Qf}}$ W	$\dot{\boldsymbol{E}}_{\boldsymbol{Qp}}$ W	$\boldsymbol{\eta_{ex}}$ $-$
Ideal case	1551.4		-494.00	372.27	0.754
Simulation	1483.4	1.3571	-447.99	277.17	0.619

The second thermal simulation is carried out with $4\,\mathrm{g\,s^{-1}}$ mass flow. For this setting blocking occurs, as depicted in <u>Fig. 5.12</u>. Analytically this operating condition should achieve output temperatures of $T_{f.out} = 746.71\,\mathrm{K}$ for the fluid and $T_{p.out} = 799.59\,\mathrm{K}$ for the particle flow, resulting in an exergetic efficiency of $73.5\,\%$.
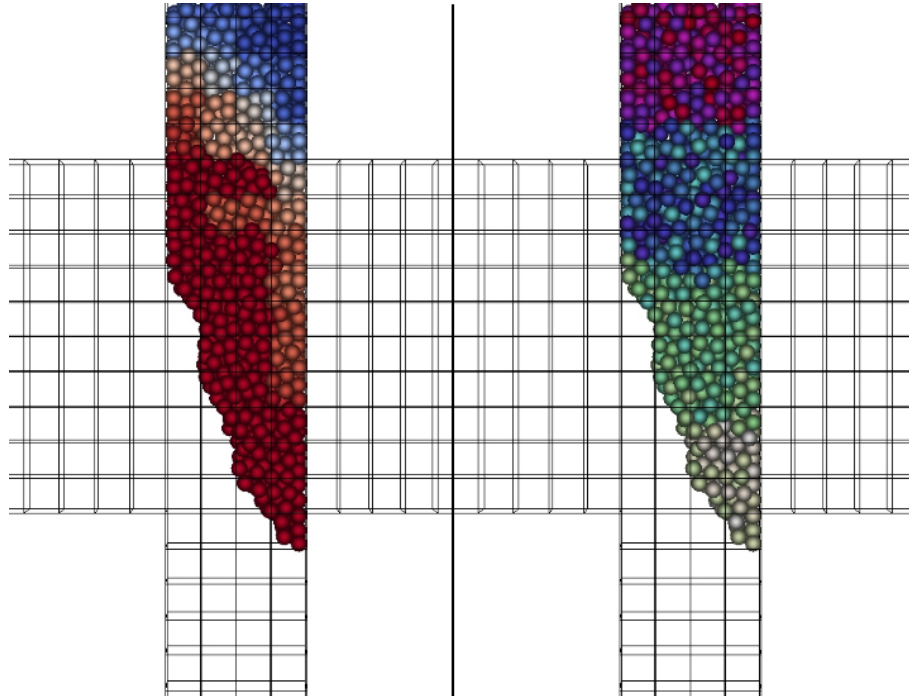
Fig. 5.12: Particle temperature distribution (hot = red; cold = blue) for granular flow with blocking effect (left) and unchanged particle layers due to blocking (right) (THERMO set-up) ($4\,\mathrm{g\,s^{-1}}$)

Nevertheless, due to the blocking no particle mass flow occurs and after the remaining sand in the heat exchange zone has heated up no further heat transfer is performed, therefore the fluid outlet temperature approaches the fluid inlet temperature. The temperature profile of the fluid is depicted in <u>Fig. 5.13</u> (p. 43) (left). The fluid shows a marginal reduction in temperature on the outlet side. At the same time the velocity profile (right) indicates that the major part of fluid mass flow passes through the bottom section of the heat exchange zone, as here the depth of the granular blocking is the smallest and provides the least resistance. Thus, the main portion of mass and with it heat passes unused through the heat exchange zone and renders the heat exchanger useless. Therefore,

no further exergetic efficiency analysis is conducted for this case, as it these operating conditions have proven to be not feasible.
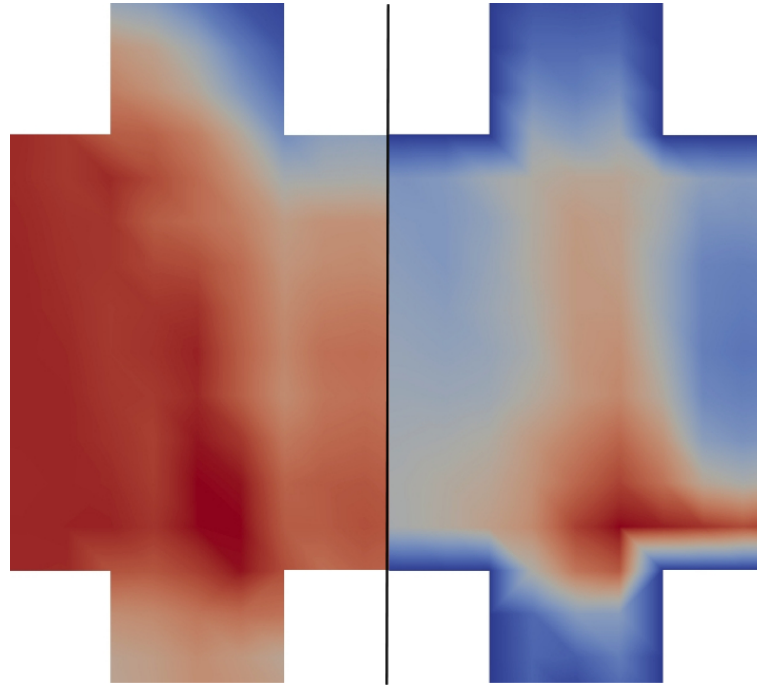
Fig. 5.13: Fluid temperature profile (hot = red; cold = blue; left) and fluid velocity profile (high = red; low = blue; right) for granular flow with blocking effect (THERMO set-up) $(4\,\mathrm{g\,s^{-1}})$.

6 Conclusion

The main focus of this work lies on the development of a simulation set–up for the Air–Sand Heat Exchanger with easily accessible open source software. The overall aim is to be able to simulate the full thermal and fluid–particle behaviour of the Air–Sand Heat Exchanger.

The software used for the coupled CFD–DEM simulation is the open source package CFDEMcoupling, which accesses the CFD code of OpenFOAM and the DEM code of LIGGGHTS to join them and exchange data in one coupled simulation.

The results gained by the simulation prove that the performed coupled CFD–DEM with a quasi 2D model is able to produce pressure gradient results close to measured data ("5.1 Validation of Simulation Set–Up"). It is also capable of describing the impact of the fluid flow on the particle mass flow and the emerging granular flow effects ("5.2 Granular Flow Effects"). The simulation results have not shown the granular effects in the expected intensity of the experimental work, but the sensitivity analyses indicates that this is very likely due to the assumed friction coefficients differing from the actual material properties ("5.3 Sensitivity Analysis").

The qualitatively conducted thermal simulation first of all shows that the heat exchange behaviour between fluid and particles can be described in dependence of the granular flow effects (5.4 Temperature Transfer under Flow Effects).

Secondly, the results of the thermal simulation for different operating conditions shows the importance for coupled CFD–DEM simulation: In a basic CFD simulation with the particle column defined as a porous solid block the impact the high fluid mass flows have on the particle packing are neglected. It would simulate an acceptable heat transfer, when in reality no further heat transfer takes place as blocking occurs and the particle mass flow has stalled. Also, a basic CFD simulation cannot account for the minor particle layer deformations at low fluid mass flows (pinning) and the resulting decrease in heat exchange efficiency.

Nevertheless, the higher accuracy in predicting the fluid–particle interaction comes at the price of high computing times, as each involved particle and its interaction with other particles and the fluid phase has to be calculated separately. But still, it is possible to reduce the computing times by setting up a model displaying a fraction of the actual problem and using periodic boundary conditions and symmetries.

In addition to the high computing times the next problem of the DEM simulation is the setting of particle properties. For a correct calculation of the particle and fluid interactions the particle properties (and surface properties for wall–particle interactions) must be known, otherwise the results differ greatly from experimental and expected data.

Overall CFDEMcoupling is shown to be an acceptable tool for CFD-DEM simulation, when all necessary parameters are known.

The next step in development is to transfer the findings of this work to the circular heat exchanger set–up to be able to analyse the granular flow effects within, as the model set–up does not allow for visual observations. But before this step is taken, the material properties must be sufficiently determined and maybe additional investigations conducted towards the stability of the particle sizes (increase of fine particles during operation) and their effect on the separating grid (clogging) as these effects were not analysed in this work. Additionally, a quantitative thermal CFD–DEM simulation should be carried out and compared to experimental data, as the thermal simulation performed in this work is based on a qualitatively approach.

A Appendix

A.1 Particle Diameter

The particle diameter used in the simulations is obtained from the grain size distribution for quartz sand with a graining of $2.0 - 3.15\,\text{mm}$ provided by **M + E Tebbe-Neuenhaus GmbH & Co.KG**.

Grain size distribution for graining $2.0 - 3.15\,\text{mm}$ [19]

Test sieves	Percentage Residue	Percentage Passing
mm	%	%
0.000	1.02	0.00
1.800	4.41	1.02
2.000	16.08	5.43
2.240	71.56	21.51
2.800	6.33	93.07
3.000	0.48	99.40
3.150	0.10	99.88
3.350	0.02	99.98

To gain the particle diameter the residues of the particles x_i is divided by the respective sieve sizes $d_p i$ and summed up. The equivalent particle diameter d_k then is described as

$$d_k = \frac{1}{\sum \left(x_i / d_p i \right)}. \tag{A.1}$$

A.2 Rectangular Ducts − Equivalent Diameter

According to American Society of Heating [cf. 2, p. 34.8] the generally applied *hydraulic diameter D_h*

$$D_h = \frac{4A}{P}, \tag{A.2}$$

for noncircular ducts can lead to inconsistencies, especially when solving for laminar flows (A being the duct area and P the perimeter of cross section). Therefore it is recommended to make use of the relationship between rectangular and round ducts as stated by *Huebscher (1948)*:

$$D_e = \frac{1.30 \left(ab \right)^{0.625}}{\left(a + b \right)^{0.250}}, \tag{A.3}$$

where D_e is the circular equivalent diameter, a the length of one side of the duct, and b the length of the adjacent side of the duct.

With this relationship the circular equivalent diameter for equal flow characteristics can be determined.

For the simulation the superficial velocities had to be adapted. Using the same velocities as measured in the laboratory the simulated pressure difference would significantly deviate from the measured one. The rectangular duct had to be transferred to a round duct and the modified superficial velocities derived from the unchanged mass flow.

Calculations with the air duct dimensions $a = 0.14$m and $b = 0.043$m and the air mass flow

$$\dot{m}_f = u_{free} A \rho_f \tag{A.4}$$

—first determing the mass flow for the rectangular duct (should be in range of measurements), then applying the equivalent diameter—lead to the identification of a modification factor for the superficial velocities $f_{mod} = 1.157$.

A.3 CFD − blockMeshDict and Patches Code

Listing A.1: blockMeshDict for simulation based on VA3

```
1  FoamFile
2  {
3      version         2.0;
4      format          ascii;
5      class           dictionary;
6      object          blockMeshDict;
7  }
8  // *********************************************//
9  //————————————————————————————————————————————
10 // TOP SECTION − Variables
11 //————————————————————————————————————————————
12
13 //Step 1 − Dimensions
14 //Conversion to fit dimensions, if needed
15 convertToMeters 1;
16
17 //Step 2 − Defining variables
18 //Points x−direction
19 xIn  −0.5;
20 xInField 0;
21 xOutField 0.046;
```

```
22  xOut 0.546;
23
24  //Number of cells in x-direction
25  xBlockI 100;
26  xBlockII 9;
27  xBlockIII 109;
28
29  //Points in y-direction
30  zTop 0.34;
31  zBottom 0.2;
32  zSandBottom 0;
33  zSandTop 0.6;
34
35  //Number of cells in z-direction
36  zBlockI 40;
37  zBlockII 28;
38  zBlockIII 48;
39
40  //Points in y-direction
41  yFront 0;
42  yBack 0.00557;
43
44  //Number of cells in y-direction
45  yBlockI 1;
46
47  //Gradings in x,y and z-direction
48  XBLI 1;
49  XBLII 1;
50  XBLIII 1;
51
52  YBLI 1;
53
54  ZBLI 1;
55  ZBLII 1;
56  ZBLIII 1;
57
58  //——————————————————————————————————
59  // BOTTOM SECTION - Fixed
60  //——————————————————————————————————
61
62  //Step 3 - Creating the vertices
63  vertices
64  (
65  //Vertices for Block I to adjoining Block II
66      ($xIn         $yFront $zBottom) //0
67      ($xInField    $yFront $zBottom) //1
68      ($xInField    $yBack  $zBottom) //2
```

```
69          ($xIn              $yBack  $zBottom)  //3
70          ($xIn              $yFront $zTop)     //4
71          ($xInField         $yFront $zTop)     //5
72          ($xInField         $yBack  $zTop)     //6
73          ($xIn              $yBack  $zTop)     //7
74  //Remaining vertices of Block II (and shared with adjoining
        ↪ Block III)
75          ($xOutField        $yFront $zBottom)  //8
76          ($xOutField        $yBack  $zBottom)  //9
77          ($xOutField        $yBack  $zTop)     //10
78          ($xOutField        $yFront $zTop)     //11
79  //Remaining vertices of Block III
80          ($xOut             $yFront $zBottom)  //12
81          ($xOut             $yBack  $zBottom)  //13
82          ($xOut             $yBack  $zTop)     //14
83          ($xOut             $yFront $zTop)     //15
84  //Remaining vertices of Block IV
85          ($xInField         $yFront $zSandBottom)  //16
86          ($xOutField        $yFront $zSandBottom)  //17
87          ($xOutField        $yBack  $zSandBottom)  //18
88          ($xInField         $yBack  $zSandBottom)  //19
89  //Remaining vertices of Block V
90          ($xInField         $yFront $zSandTop)  //20
91          ($xOutField        $yFront $zSandTop)  //21
92          ($xOutField        $yBack  $zSandTop)  //22
93          ($xInField         $yBack  $zSandTop)  //23
94  );
95
96  //Step 4 - Creating the blocks
97  blocks
98  (
99          hex (0 1 2 3 4 5 6 7) ($xBlockI $yBlockI $zBlockII)
                ↪ simpleGrading ($XBLI $YBLI $ZBLII)
100         //Block I
101         hex (1 8 9 2 5 11 10 6) ($xBlockII $yBlockI $zBlockII)
                ↪ simpleGrading ($XBLII $YBLI $ZBLII)
102         //Block II
103         hex (8 12 13 9 11 15 14 10) ($xBlockIII $yBlockI
                ↪ $zBlockII) simpleGrading ($XBLIII $YBLI $ZBLII)
104         //Block III
105         hex (16 17 18 19 1 8 9 2) ($xBlockII $yBlockI $zBlockI)
                ↪ simpleGrading ($XBLII $YBLI $ZBLI)
106         //Block IV
107         hex (5 11 10 6 20 21 22 23) ($xBlockII $yBlockI
                ↪ $zBlockIII) simpleGrading ($XBLII $YBLI $ZBLIII)
108         //Block V
109
```

```
110  ) ;
111
112  //Step  5 − Defining  of  boundaries
113  boundary
114  (
115          inflow
116          {
117              type patch ;
118              faces
119              (
120                  (0  3  7  4)
121              ) ;
122          }
123          outflow
124          {
125              type patch ;
126              faces
127              (
128                  (12  13  14  15)
129              ) ;
130          }
131          walls
132          {
133              type  wall ;
134              faces
135              (
136                  (4  5  6  7)        //2
137                  (0  1  2  3)        //4
138                  (1  16  19  2)      //5
139                  (5  6  23  20)      //6
140                  (17  18  9  8)      //13
141                  (11  10  22  21)    //14
142                  (11  15  14  10)    //16
143                  (8  12  13  9)      //18
144              ) ;
145          }
146          SandInAndOut
147          {
148              type  slip ;
149              faces
150              (
151                  (16  17  18  19)    //Bottom
152                  (20  21  22  23)    //Top
153              ) ;
154          }
155          frontAndBack
156          {
```

```
157              type empty;
158              faces
159              (
160                  (0  1  5  4)         //1
161                  (1  8  11  5)        //8
162                  (8  12  15  11)      //15
163                  (16  17  8  1)       //7
164                  (5  11  21  20)      //9
165                  (3  2  6  7)         //3
166                  (2  9  10  6)        //11
167                  (9  13  14  10)      //17
168                  (19  18  9  2)       //10
169                  (6  10  22  23)      //12
170              );
171          }
172  );
173
174  mergePatchPairs
175  (
176  );
177
178  // ***************************************************//
```

A.4 DEM − Simulation Code

Listing A.2: DEM initial simulation code for sand column with layer colouring and temperature, based on VA3

```
1  units             si                 # SI units are used
2  atom_style        sphere             # particles are spheres
3  atom_modify       map array
4  boundary          f  p  f            # x,y,z dimension boundaries (f
   ↪ = fix , p = periodic)
5  newton            off
6  communicate       single vel yes
7
8  # parameters of simulation box (x x y y z z); units box ->
   ↪ values are in SI units
9  region            domain block 0 0.046 0 0.00557 0. 2. units box
10 create_box        2 domain           # two materials wihtin
   ↪ simulation box
11
12 neighbor          0.002 bin
13 neigh_modify      delay 0
14
15 # material properties (material1, material2)
```

```
16 fix                 m1 all property/global youngsModulus peratomtype
   ↪   74e7 200e7
17 fix                 m2 all property/global poissonsRatio peratomtype
   ↪   0.12 0.3
18 # material properties (two materials, mat1-mat1, mat1-mat2, mat2
   ↪ -mat1, mat2-mat2)
19 fix                 m3 all property/global coefficientRestitution
   ↪ peratomtypepair 2 0.7 0.8 0.8 0.9
20 fix                 m4 all property/global coefficientFriction
   ↪ peratomtypepair 2 0.7 0.8 0.8 0.3
21
22 # granular model
23 pair_style        gran model hertz tangential history #Hertzian
   ↪ without cohesion
24 pair_coeff        * *
25
26 # time step, depends on Rayleigh Time
27 timestep          0.000001
28
29 # gravity vector
30 fix                 gravi all gravity 9.81 vector 0.0 0.0 -1.0
31
32 # heat transfer properties (material1, material2)
33 fix                 ftco all property/global thermalConductivity
   ↪ peratomtype 5. 50.
34 fix                 ftca all property/global thermalCapacity
   ↪ peratomtype 0.1 460
35 # initial temperature of particles
36 fix                 heattransfer all heat/gran initial_temperature
   ↪ 273
37 # set general colouring of particles
38 fix                 color all property/atom Color scalar yes no no 0
39
40 # particle properties and distribution
41 fix                 pts1 all particletemplate/sphere 1 atom_type 1
   ↪ density constant 2650 radius constant 0.001114
42 fix                 pdd1 all particledistribution/discrete 1. 1 pts1
   ↪   1      # only one type of particle
43
44 # insertion of CAD parts of quasi 2D model of heat exchanger
45 fix                 cad all mesh/surface file mesh/airinout.stl type
   ↪   2
46 fix                 cad2 all mesh/surface file mesh/sandout.stl type
   ↪   2 move 0. 0. 0.15      # CAD part is moved up vertically
47 fix                 geometry all wall/gran model hertz tangential
   ↪ history mesh n_meshes 2 meshes cad cad2   # parts defined
   ↪ as walls
```

```
48
49 # particle insertion
50 fix                inlet all mesh/surface file mesh/sandin.stl type
      ↪  2
51 fix                ins1 all insert/stream seed 1000
      ↪ distributiontemplate pdd1 nparticles 10000 vel constant 0.
      ↪  0. −0.5 particlerate 1000 overlapcheck yes insertion_face
      ↪  inlet extrude_length 1
52
53 # apply nve integration to all particles that are inserted as
      ↪ single particles
54 fix                integr all nve/sphere
55
56 # output settings, include total thermal energy
57 compute            1 all erotate/sphere
58 thermo_style       custom step atoms ke c_1 vol
59 thermo             1000
60 thermo_modify      lost ignore norm no
61 compute_modify     thermo_temp dynamic yes
62
63 # insert the first particles so that dump is not empty
64 fix                ctg all check/timestep/gran 1 0.01 0.01
65 run                1
66 unfix              ctg
67
68 # dump data every 10000 steps
69 dump               dmp all custom 10000 post/dump*.3c3_init id type
      ↪  type x y z ix iy iz vx vy vz radius f_Temp[0] f_heatFlux
      ↪  [0]
70
71 # run time until next step
72 run                990000 upto
73
74 # group particles according to their ID number
75 group              col1 id <= 1000
76 group              col2 id 1001:2000
77 group              col3 id 2001:3000
78 group              col4 id 3001:4000
79 group              col5 id 4001:5000
80 group              col6 id 5001:6000
81 group              col7 id 6001:7000
82 group              col8 id 7001:8000
83 group              col9 id 8001:9000
84 group              col10 id 9001:10000
85
86 # colour particles according to their group
87 set group col1 property/atom Color 1
```

```
88 set  group  col2  property/atom  Color  2
89 set  group  col3  property/atom  Color  3
90 set  group  col4  property/atom  Color  4
91 set  group  col5  property/atom  Color  5
92 set  group  col6  property/atom  Color  6
93 set  group  col7  property/atom  Color  7
94 set  group  col8  property/atom  Color  8
95 set  group  col9  property/atom  Color  9
96 set  group  col10  property/atom  Color  10
97
98 # run  time
99 run                     10000
100
101 # write  restart  file  for  further  simulations
102 write_restart    ../DEM/3c3.restart
```

Listing A.3: DEM resume simulation code for sand mass flow with layer colouring and temperature, based on VA3

```
1 # the  simulation  is  resumed  from  previously  created  restart  file
2 read_restart    ../DEM/3c3.restart
3
4 neighbor          0.002  bin
5 neigh_modify     delay  0
6
7 # particle  properties  (values  can  be  changed)
8 # granular  model,
9 # time  step,
10 # gravity,
11 # heat  transfer  properties  (can  be  changed)
12 # as  initial  simulation  code
13
14 # set  particle  temperature  for  the  bed
15 run  0
16 region   total  block  INF  INF  INF  INF  INF  INF  units  box
17 set       region  total  property/atom  Temp  473.15
18
19 # insertion  of  CAD  parts  of  quasi  2D  model  of  heat  exchanger  as
     ↪ initial  simulation  code
20
21 # set  general  parameters  for  CFD–DEM  coupling
22 fix      cfd  all  couple/cfd  couple_every  1000  mpi         #
     ↪ overwritten  by  "couplingProperties"
23 fix      cfd2  all  couple/cfd/force                          # CFD
     ↪ forces  on  particles
24 fix      cfd3  all  couple/cfd/convection  T0  473.15         # effect
     ↪ of  particle  temp.  an  CFD
25
```

```
26 # particle insertion and nve integration as initial simulatin
      ↪ code
27
28 # mimicing mass flow, vertical movement of stopper (cad2) in m/s
29 fix        stopper all move/mesh mesh cad2 linear 0.0 0.0 -0.002843
30
31 # output settings and first particle insertion to dump as
      ↪ initial simulation code
32
33 # parameters to be dumped
34 dump       dmp all custom 100000 ../DEM/post/dump*.18_505 id type
      ↪ type x y z vx vy vz fx fy fz f_dragforce[1] f_dragforce[2]
      ↪  f_dragforce[3] radius f_Temp[0] f_heatFlux[0]
```

A.5 P-NTU Method Code

Listing A.4: P-NTU Method Code for determing fluid and particle outlet temperture

```
1 %****************************************************************%
2 % Temperature change (analytical)
3 %****************************************************************%
4
5 %══════════════════════════════════════════════════════════════
6 % Comparison with VA4 (2-3.15 mm) for 200degC - 800degC
7 %══════════════════════════════════════════════════════════════
8
9 % Inlet temperatures for fluid and particles
10 t_fi = 800+273.15;
11 t_pi = 200+273.15;
12
13 % Properties of particle (Quartz)
14 d_mm = 2.228;            % mean diameter in mm
15 d_k = d_mm/1000;         % mean diameter in m
16 V_p = 1/6 * pi * d_k^3; % volume of single particle in m^3
17 rho_p = 2650;           % particle density in kg/m^3
18 c_pp = 1050             % particle heat capacity in J/(kgK)
19 lambda_p = 5.8565       % conductivity in W/(mK)
20
21 % Properties of fluid (Air)
22 w_free = 4.1736;        % superficial velocity in x-direction
23 rho_f = 0.53719         % fluid density in kg/m^3
24 c_pf = 1091.0167        % fluid heat capacity in J/(kgK)
25 lambda_f = 0.054089     % conductivity in W/(mK)
26 eta = 0.000035933       % dyn. viscosity in kg/(ms)
27 nu = eta/rho_f          % kin. viscosity in m^2/s
28
```

```
29 % Heat exchange zone
30 a = 0.05;                    % height of heat exchange zone in m
31 b = 0.02;                    % widht of heat exchange zone in m
32 c = 0.00557;                 % depth of heat exchange zone in m
33 V_zone = a * b * c;          % volume of heat exchange zone in m^3
34 epsilon = 0.40;              % voidfraction of bulk solids
35 factor = c_pf/c_pp;          % factor to compensate differences
36                              % in heat capacity rate
37 m_fg = 2;
38 m_f = m_fg/1000;
39 m_p = m_f;
40
41 %================================================
42 % Calculation of heat coefficients
43 %================================================
44
45 % Heat transfer coeffizient alpha
46 Re = (w_free * d_k)/(nu * epsilon);       % Reynolds number
47 Pr = (eta * c_pf)/lambda_f;               % Prandtl number
48 Nu_lam = 0.664 * sqrt(Re) * nthroot(Pr,3);       % Nusselt number
49                                           % for laminar part
50 Nu_turb = (0.037 * Re^(0.8) * Pr)/(1 + 2.443 * Re^(-0.1) * (Pr
     ↪ ^(2/3) - 1)); % Nusselt number turbulent part
51 Nu_single = 2 + sqrt(Nu_lam^2 + Nu_turb^2);       % Nusselt number
52                                           % for single particle
53 Nu = (1 + 1.5 * (1-epsilon))* Nu_single;
54 alpha = (Nu * lambda_f)/d_k
55
56 % Biot number
57 Bi = alpha * d_k / lambda_p
58
59 %================================================
60 % Calculation of exit temperature of fluid (P - NTU Method)
61 %================================================
62
63 A_p = d_k^2 * pi;                          % particle surface
64 no_p = (V_zone*(1-epsilon))/V_p;           % number of particles
65 a_p = no_p * A_p;         % overall particle surface (bulk solids)
66 W = m_f*c_pf;             % heat capacity rate
67 NTU = (alpha * a_p)/W     % Number of Transfer Units
68
69 P = 1 / ( 1/(1 - exp(-NTU)) + 1/(1 - exp(-NTU)) - 1/NTU)
70 % temperature effectiveness
71
72 t_fo = t_fi - P * (t_fi - t_pi) % resulting fluid outlet
     ↪ temperature
```

```
73 t_po = t_pi + P * (t_fi − t_pi) % resulting particle outlet
   ↪ temperature
74
75 %═══════════════════════════
76 % Exergetic Efficiency
77 %═══════════════════════════
78
79 T_amb = 298.15;          % ambient temperature in K
80 R = 287.10;              % gas constant for dry air in J/(kgK)
81 kappa = c_pf / (c_pf − R)      % heat capacity ratio
82
83 u = w_free/1.121;
84
85 dp = ( 150*(nu*rho_f*u)/d_k^2*(1−epsilon)^2/epsilon^3 +
86                 1.75*(rho_f*u^2)/d_k*(1−epsilon)/epsilon^3 ) * b
87                      % Ergun Equation
88
89 % Calculations for ideal case
90 p2 = 101325;             % ambient pressure in Pa (at outlet)
91 p1 = p2 + dp;            % pressure at inlet
92
93 E_Qf = −m_f*c_pf*(t_fi−t_fo)−T_amb*(m_f*c_pf*(log(t_fo/t_fi)−(
   ↪ kappa−1)/kappa*log(p2/p1)))
94 % Exergy flow of heat flow released by fluid
95 E_Qp = m_p*c_pp*(t_po−t_pi)−T_amb*m_p*c_pp*log(t_po/t_pi)
96 % Exergy flow of heat flow received by particles
97 eta_ex = E_Qp/−E_Qf      % Exergy efficiency
98
99 % Calculations for simulated case
100 t_pos = 737.45;
101 t_fos = 770.01;
102 dp_s = 1483.4;
103
104 p1s = p2 + dp_s;
105
106 E_Qfs = −m_f*c_pf*(t_fi−t_fos)−T_amb*(m_f*c_pf*(log(t_fos/t_fi)
    ↪ −(kappa−1)/kappa*log(p2/p1s)))
107 E_Qps = m_p*c_pp*(t_pos−t_pi)−T_amb*m_p*c_pp*log(t_pos/t_pi)
108 eta_ex = E_Qps/−E_Qfs
```

Bibliography

[1] International Energy Agency. <u>Praktische Physik</u>. IEA Publications, Paris, 2012.

[2] Refrigerating & A-C Engineers American Society of Heating. <u>2001 ASHRAE Fundamentals Handbook (SI)</u>. ASHRAE, Atlanta, GA, SI edition, 2001.

[3] J. M. Boac, M. E. Casada, R. G. Maghirang, and J. P. Hamer III. 3-D and Quasi-2-D Discrete Element Modeling of Grain Commingling in a Bucket Elevator Boot System. <u>Transactions of the ASABE</u>, 55(2):659–672, 2012.

[4] C. S. Campbell. Granular material flows — An overview. <u>Powder Technology</u>, 162 (3):208–229, 2006.

[5] G. Cerbe and G. Wilhelms. <u>Technische Thermodynamik — Theoretische Grundlagen und praktische Anwendungen</u>. Carl Hanser Verlag, München, 16$^{\text{th}}$ edition, 2011.

[6] Y. CHEN, X. ZHU, Y. WU, and Z. ZHU. The investigation of pressure drop in moving-beds. <u>Frontiers of Chemical Engineering in China</u>, 1(2):184–189, 2007.

[7] DCS Computing GmbH Christoph Goniva. <u>CFDEMcoupling Documentation</u>, 2012.

[8] OpenFOAM Foundation. <u>OpenFOAM – The Open Source CFD Toolbox</u>, 2.3.0 edition, February 2014.

[9] C. Goniva, C. Kloss, A. Hager, and S. Pirker. An Open Source CFD-DEM Perspective, 2010.

[10] B. S. Hemingway. Quartz: Heat capacities from 340 to 1000 K an revised values for the thermodynamic properties. <u>American Mineralogist</u>, 72:273–279, 1987.

[11] W. Hemming and W. Wagner. <u>Verfahrenstechnik</u>. Vogel Industrie Medien GmbH & Co. KG, Würzburg, 10$^{\text{th}}$ edition, 2008.

[12] K. Hilfiker, L. Gasser, and B. Wellig. Energieumwandlungen mit Exergie–Analyse richtig bewerten. In <u>14. Tagung des BFE–Forschungsprogramms Umgebungswärme</u>, pages 75–86, 2007.

[13] International Energy Agency. Technology Roadmap — Concentrating Solar Power. Technical report, International Energy Agency, 2010.

[14] Karl Jungbluth Kettenfabrik GmbH & Co. KG. Technische Auslegung. `http://www.jungbluth-ketten.de/GER/download/download_00.html`, November 2014.

[15] C. Kloss, C. Goniva, A. Hager, S. Amberger, and S Pirker. Models, algorithms and validation for opensource DEM and CFD-DEM. Progress in Computational Fluid Dynamics, An. Int. J, 12(2/3):140–152, 2012.

[16] F. Kohlrausch. Praktische Physik, volume 1. B. G. Teubner, Stuttgart, 24th edition, 1996.

[17] H.-J. Kretzschmar and I. Kraft. Kleine Formelsammlung Technische Thermodynamik. Carl Hanser Verlag, München, 2nd edition, 2008.

[18] S. Lecheler. Numerische Strömungsberechnung. Vieweg + Teubner, Wiesbaden, 2009.

[19] M + E Tebbe-Neuenhaus GmbH & Co.KG. Produktdatenblatt. `http://www.tebbe-neuenhaus.de/quarzsand/`, November 2014.

[20] R. Marek and K. Nitsche. Praxis der Wärmeübertragung. Hanser, München, 2007.

[21] S. Niederwestberg. Schüttgut-Rheologie und Luftsrom-Charakteristik im Luft-Sand-Wärmeübertrager, Messungen und Theorie. B.eng. thesis, Fachhochschule Nordhausen — University of Applied Sciences, 2014.

[22] K. A. Pilcher and J. Bridgwater. Pinning in a Rectangular Moving Bed Reactor with Gas Cross–Flow. Chemical engineering science, 45(8):2535–2542, 1990.

[23] W. Polifke and J. Kopitz. Wärmeübertragung — Grundlagen, analytische und numerische Methoden. Pearson Studium, München, 2nd edition, 2009.

[24] M. Rhodes. Introduction to Particle Technology. Wiley, Chichester, 2nd edition, 2008.

[25] D. Schulze. Pulver und Schüttgüter — Fliesseigenschaften und Handhabung. Springer, Berlin, 2nd edition, 2009.

[26] R. K. Shah and D. P. Sekulić. Fundamentals of Heat Exchanger Design. Wiley, Hoboken, New Jersey, 2003.

[27] E. M. Smuts, D. A. Deglon, and C. J. Meyer. Methodology for CFD-DEM Modelling of Particulate Suspension Rheology. In Ninth International Conference on CFD in the Minerals and Process Industries, 2012.

[28] J. Sykut, M. Molenda, and J. Horabik. Discrete Element Method (DEM) as a Tool for Investigating Properties of Granular Materials. Polish Journal of Food and Nutrition Sciences, 57(2):169–173, 2007.

[29] United Nations Framework Convention on Climate Change. About UNFCCC. `http://newsroom.unfccc.int/about/`, November 2014.

[30] Verein Deutscher Ingenieure. VDI–Wärmeatlas: mit 320 Tabellen. VDI-Buch. Springer Vieweg, Berlin, 11$^{\text{th}}$ edition, 2013.

[31] T. Westermann. Modellbildung und Simulation — Mit einer Einführung in ANSYS. Springer, Berlin, 2010.

[32] Y.-G. Yoon, R. Car, D. J. Srolovitz, and S. Scandolo. Thermal conductivity of crystalline quartz from clissical simulations. Physical Review B, 70:012302–1–012302–4, 2004.

[33] D. Zabulionis, R. Kačianauskas, D. Markauskas, and J. Rojek. An investigation of nonlinear tangential contact behaviour of a spherical particle under varying loading. Bulletin of the Polish Academy of Sciences — Technical Sciences, 60(2):265–278, 2012.

[34] J. Zhao and T. Shan. Coupled CFD-DEM simulation of fluid-particle interaction in geomechanics. Powder Technology, 239:248–258, 2013.

Erklärung

Hiermit versichere ich, dass ich diese Arbeit selbständig verfasst und keine anderen als die anÂgegebenen Quellen und Hilfsmittel benutzt habe. Außerdem versichere ich, dass ich die allgemeinen Prinzipien wissenschaftlicher Arbeit und Veröffentlichung, wie sie in den Leitlinien guter wissenschaftlicher Praxis der Carl von Ossietzky Universität Oldenburg festgelegt sind, befolgt habe.

Jacqueline McLeod